

A Remote Sensor for Marine Mammal Localization

submitted by

Ehsan Malekshahi

Jordin McEachern

Adam Forget

Mark Watson

Nikola Doelle

Cole Ferguson

Shadi Aljendi

Jean-François Bousquet

Dalhousie University

June 2021

Contents

1	Project Objectives	3
2	Localization	4
2.1	Background	4
2.2	Propagation Models	6
2.2.1	Coordinate Systems	6
2.2.2	The Acoustic Propagation Model	9
2.3	Frequency-Domain Localization Algorithms	13
2.3.1	MUSIC localization method	13
2.3.2	MSE localization method	14
2.3.3	Bartlett localization method	14
2.4	Time-Domain Localization Algorithms	15
2.4.1	MCCC localization method	15
2.4.2	MUSIC Estimator	16
2.5	Proposed Algorithm for High Frequency Localization	18
2.6	Evaluation of the Performance	22
2.6.1	Sea Trials	22
2.6.2	Estimation of bearing and range	27
2.7	Real-Time System Architecture	32
2.7.1	Firmware Architecture	32
2.7.2	Real-time Localization Implementation	38
2.7.3	Verification of the Controller in Test Tanks	43
3	Magneto-Inductive Coupling	47
3.1	Analytical Model	47
3.1.1	Initial Setup	47
3.1.2	Deep Water Solution	47
3.1.3	Crossing the Air-Water Interface	49
3.1.4	Magnetic Induction	50
3.1.5	Comparison with Gibson's Model	51
3.2	Circuit Model	53
3.3	Frequency Dependence	54
3.4	Field Experiments	54
3.4.1	Transmitter Design	54
3.4.2	Receiver Design	56
3.4.3	Test Procedure	58
3.4.4	Preliminary Data Analysis	59
4	Conclusions and Impact	64
5	Recommendations and Future Considerations	64

Executive Summary

The deployment of infrastructure in the ocean is often slowed due to the potential harm of animals in the area. In the Bay of Fundy, the deployment of tidal farms have been explored for several years, however there is a large population of harbour porpoises. In this work, a remote passive localization system is proposed to track harbour porpoises using the sound emitted by the animal. In comparison to active sonar systems, the proposed sensor does not send a pulse. This reduces the potential noise pollution, as well as the energy consumption of the system.

In order to implement this real-time system, two core components are developed: the localization algorithm, as well as the communication link to return the information to the surface. A complete design procedure is described in this report, including the analytical development, the modelling and the testing of the system.

The proposed real-time algorithm relies on a compact hydrophone array that is designed to detect bearing and range. The algorithm complexity is optimized to be programmed on a field programmable gate array (FPGA); the FPGA is used for parallel computing of the acoustic data.

The algorithm is tested using calibration data in realistic conditions, as well as with real harbour porpoise echolocation samples that were collected in the Bay of Fundy in the Summer 2019.

The communication system as well as the hardware for the localization system are deployed in the Aquatron. The analytical models, validated by the measurement results demonstrate the great potential for magneto-inductive communication as a means to cross the air-water interface. Additionally, these tests were used to confirm how the sensor array can be connected to the processor to enable real-time localization.

Overall, the developed platform has great potential as a smart remote sensor node that can be used to monitor the ocean in real-time.

1 Project Objectives

The deployment of infrastructure in the ocean has been slowed due to the concern that it may cause additional harm to endangered species, and will affect the ecosystem. Specifically, in the Bay of Fundy, there is an interest to deploy tidal turbines. However, there is large population of harbour porpoises that could be affected by the noise, and could even be harmed by the moving parts.

In this project, the objective is to develop a real-time localization system that can detect the presence of harbour porpoises using acoustic sensors within a maximum range of one kilometer. The sensors will be moored at the bottom of the ocean in proximity of the tidal equipment or attached to the fixed structure of the turbine. It is assumed that power is provided to the nodes, so that they can be deployed over extended periods of time, with minimal maintenance. Also, a communication link will be available to return events to the end user in real-time, so that informed decisions can be made. To design the localization system, an algorithm will be proposed to localize the desired acoustic signatures and to provide an accurate estimation of the range and bearing of the source. The algorithm relies at its core on an accurate representation of the propagation environment to provide a high estimation accuracy which will be programmed on a real-time processing board. The passive sensor will be implemented using an available 5-element acoustic sensor array.

The real-time localization algorithm will allow to process the data directly at the remote nodes, and avoid recording and transmitting large datasets to a remote user. To recover the information at the surface, a wireless communication link will be established between the subsea sensor, and a receiver above the sea-surface (for example an aerial drone). The wireless link to a platform above the sea surface will avoid having a buoy that can be easily damaged by the rough sea conditions.

In this report, first, localization algorithms will be described in Chapter 2 and their performance will be evaluated using a realistic dataset taken in the Bay of Fundy in the Summer 2019. Secondly, in Chapter 3, a test setup will be described to assess the performance of a magneto-inductive communication link. Finally, future work will be presented in Section 5.

2 Localization

2.1 Background

Different localization methods including the most recently developed method will be described in this document. For localization purposes, using an accurate propagation model beside an applicable localization method is very important. There are many differences between the underwater environment and the free space environment. The multi-paths appear in the underwater environment, while the single path (direct path) is the strongest path for the propagation of sound in the free space.

The localization methods can be divided into two general groups: the time-domain methods, and the frequency-domain methods. The multi-channel cross correlation coefficient (MCCC) and the multiple signal classification (MUSIC) are some of the time-domain methods [1]. They are presented for the free space, and thus they are not useful for the more complicated underwater models such as Lloyd-Mirror, Image, and Normal-modes. The underwater environment will be modeled physically as described in [2]. The results show that the MCCC method provides good resolution if the measured data are subject to a low signal-to-noise ratio (SNR) and from one source. Even in the high frequency (about 50 kHz) when a hydrophone array without short enough distances between each two elements is used (i.e. the distances between each two elements is not shorter than $\frac{\lambda}{2}$, where λ is the wavelength), the results of MCCC are still in high resolution with a very low aliasing effect. On the other hand, the frequency-domain approaches such as narrow-band MUSIC [3], and matched field processing (MFP) methods can distinguish the different sources if their frequency bands are not completely overlapped, while the time-domain approaches cannot. The MFP is often used for localization in the underwater environment [4, 5, 6]. The important advantage of the MFP is that it can be used with an arbitrary propagation model. Various methods in the field of MFP are presented. The Bartlett method [4] is the most basic and well-known approach of the MFP. Although the Bartlett method does not have the problems of the time-domain methods, it suffers from some limitations such as low resolution [7]. The minimum variance distortionless response (MVDR) is a high resolution approach of the MFP method [8, 9]. However, the MVDR method needs several snapshots to estimate the covariance matrix [7], that needs more computations and takes time.

For the detection of acoustic signatures, a single sensor can be sufficient to measure the pressure as a function of time. However, localization requires a minimum of two hydrophones, and in fact depending on the geometry of the array, it is possible to obtain the range, as well as the azimuth and elevation bearing.

Typically, the array geometry, the sound speed, the sampling frequency, the material and properties of environment, and the frequency range of the source are required. The sound speed along the North American coast (where the temperature at the surface is along 12° C, and the salinity is 35%) is approximately 1495 m/sec. In deep water, the sound speed varies as a function of depth due to the temperature, pressure and salinity variation, but for the shallow waters (on the order of 20 meters) that are considered in this project, the variation is negligible.

A standard process will be adopted to run the algorithms. Initially, acoustic data from multiple sensors will be input to the algorithm, as well as information about the acoustic physical conditions (sound speed profile, bathymetry). Different parameters for the estimator will also be provided. Then, the processor will calculate the energy of a hypothetical sound source at different locations. Effectively, the possible location of the sound source is in the area of maximum energy.

In fact, the process is shown in Fig. 1.1 and may be summarized using the following sequence:

1. The search area or space is input by the user. Then, the distances (based on the chosen physical model) from each point in the search area to each hydrophone (sensor) are calculated.
2. If a frequency domain method is chosen, the fast Fourier transform (FFT) is applied to the time domain signals to convert them to the frequency domain. The range of frequencies is defined by the user.
3. Based on the chosen physical model, the energy of the hypothetical source at each point of the search area is calculated using the chosen method. Note that, for the time domain methods, only the single path model is used to represent the physical environment.

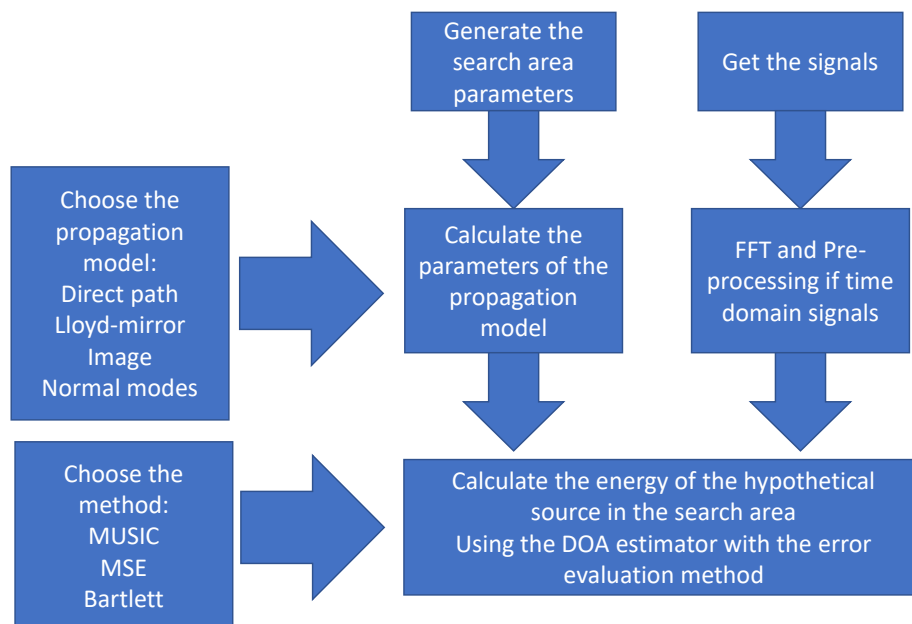


Fig. 1.1: General Structure for the Localization Algorithm.

The rest of this chapter is organized as follows. First, in Section 2.2, the physical models adopted will be described, then in Section 2.3, frequency domain localization algorithms will be presented, and in Section 2.4 time domain localization algorithms will be presented. Then, the proposed hybrid localization algorithm will be presented in Section 2.5. Finally, the localization accuracy will be evaluated in Section 2.6.

2.2 Propagation Models

To reduce the localization error, an accurate representation of the propagation environment can be taken into account. In this Chapter, first, three different coordinate systems will be presented in Section 2.2.1. Then, in Section 2.2.2, four different models of the propagation environment will be derived.

2.2.1 Coordinate Systems

Figs. 2.2.1 and 2.2.2 respectively show the top view and the side view of a planar hydrophone array that is mounted horizontally.

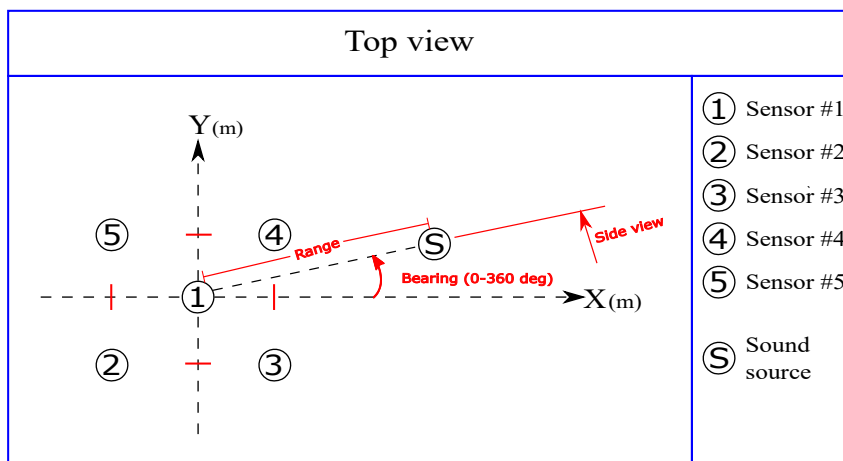


Fig. 2.2.1: Top view of a planar hydrophone array that is mounted horizontally.

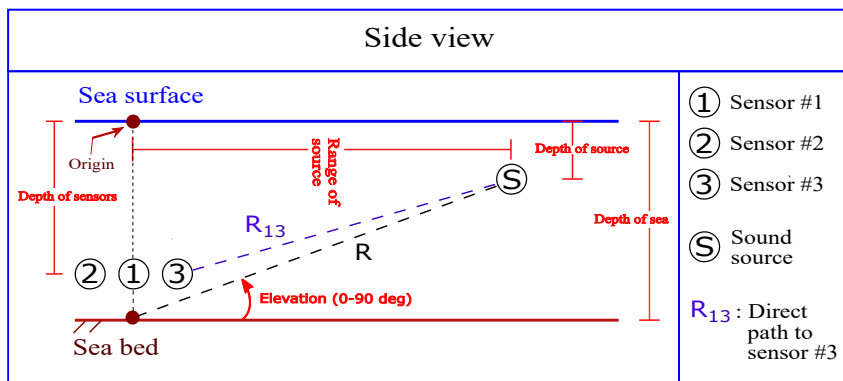


Fig. 2.2.2: Side view of a planar hydrophone array that is mounted horizontally.

Typically, the location of an acoustic source is estimated at an array of sensors. To estimate the location of the source, the subsea environment is bounded and its position can be represented using different coordinate systems. Three possible coordinate systems are considered in this document, and defined as:

1. A 3D rectangular system (X , Y and depth D)
2. A cylindrical coordinate system described by the range (R), bearing B and depth D

3. A spherical coordinate system defined by elevation (E), bearing (B) and depth (D)

Based on the chosen coordinate system, the parameters for the search space are defined as shown in Table 1. It should be noted that the bearing in degrees is defined between $0 < \phi < 360$, while the elevation in degrees is defined between $0 < \theta < 90$.

Table 1: Parameters for each coordinated system

Coordinate system	XYD	RBD	EBD
First parameter	x	r	θ
Second parameter	y	ϕ	ϕ
Third parameter	z	z	z

Note that z is the depth from the sea surface, and r is the horizontal range from the origin taken as the position of the middle of the sensor array.

The XYD coordinate system is considered as the standard coordinate system for use in the localization algorithms. Therefore, the parameters of the defined search space will be converted to the parameters of the XYD coordinate system. The point $p = (x, y, z)$ in the XYD system is equivalent to the point $p = (r, \phi, z)$ in the RBD system and the point $p = (\theta, \phi, z)$ in the EBD system if the following equations hold.

$$\begin{aligned}
 \text{RBD to XYD : } & x = r \cos(\phi), \quad y = r \sin(\phi), \\
 \text{EBD to XYD : } & x = \frac{D - z}{\tan(\theta)} \cos(\phi), \quad y = \frac{D - z}{\tan(\theta)} \sin(\phi),
 \end{aligned} \tag{1}$$

where D is the Depth of sea.

Note that in a shallow water environment, it is difficult to resolve the elevation, particularly since the proposed array geometry is horizontal. As such, the EBD coordinate system will not be utilized in this work.

Fig. 2.2.3 shows the search space in the XYD and RBD coordinate systems. If we look at the search space from the top, using the XYD coordinate system, we can see a rectangle of dimensions $y_2 - y_1$ and $x_2 - x_1$ meters. In contrast, using the RBD coordinate section, the search space can be represented as the arc of a doughnut with an inner radius of r_1 meters and an outer radius of r_2 meters, with bearings from ϕ_1 to ϕ_2 degrees. For a predefined search area, the XYD system can provide more resolution than the RBD. However, the RBD coordinate system can be defined to be sampled at an optimal resolution defined by the sensor geometry.

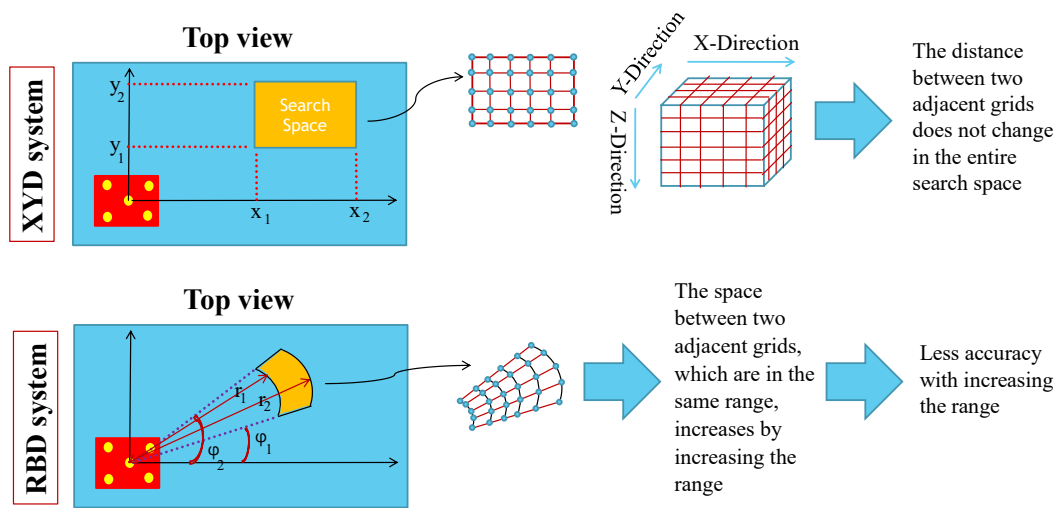


Fig. 2.2.3: The Search Space in the XYD and RBD Coordinate Systems.

2.2.2 The Acoustic Propagation Model

In this section, a low-complexity propagation model will be described to represent the propagation environment. In this work, it is assumed that the sound speed profile is constant. Let's assume that $S(\omega)$ is the transmit signal amplitude for a given acoustic source at the angular frequency ω and located at point $p_0 = (x_0, y_0, z_0)$ (in the XYD coordinate system). For a hydrophone array with N elements, the received signal $H_n(\omega)$ at the n^{th} element with the location $p_n = (x_n, y_n, z_n)$ has a relationship with $S(\omega)$ depending on the propagation model.

Single path model Assuming a free space environment, the received signal amplitude at hydrophone n is

$$H_n(\omega) = S(\omega) \times G(p_0, p_n, \omega) = -\frac{S(\omega) e^{-ikr_n}}{4\pi r_n} \quad (2)$$

where i is the imaginary unit. Also, r_n is the distance between the source and n^{th} hydrophone. Thus

$$r_n = \sqrt{(x_0 - x_n)^2 + (y_0 - y_n)^2 + (z_0 - z_n)^2}, \quad k = \omega/c, \quad \omega = 2\pi f, \quad (3)$$

where k , c , and f are the wave number, the sound speed and the frequency, respectively. Expressing the transmit signal $s(t)$ in the time-domain, the received signal can be expressed as

$$h_n(t) = -\frac{1}{4\pi r_n} \cdot s(t - \tau), \quad (4)$$

where τ is the time delay calculated as $\tau = r_n/c$.

Lloyd-mirror model The Lloyd-mirror model described in [2] and represented in Fig. 2.2.4, describes the received signal as the combination of the direct path $r_{1,n}$ with a second path $r_{2,n}$ that bounces from the sea surface.

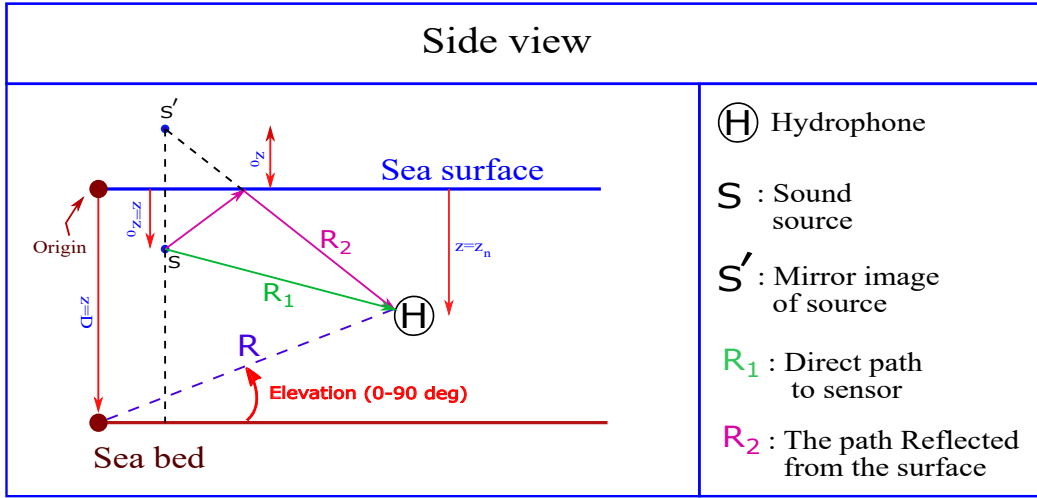


Fig. 2.2.4: Representation of the Lloyd-mirror model.

Using the Lloyd-mirror model, the received signal at hydrophone n is

$$H_n(\omega) = S(\omega) \times G(p_0, p_n, \omega) = -\frac{S(\omega)}{4\pi} \times \left(\frac{e^{-ikr_{1,n}}}{r_{1,n}} - \frac{e^{-ikr_{2,n}}}{r_{2,n}} \right) \quad (5)$$

$$r_{1,n} = \sqrt{(x_0 - x_n)^2 + (y_0 - y_n)^2 + (z_0 - z_n)^2},$$

$$r_{2,n} = \sqrt{(x_0 - x_n)^2 + (y_0 - y_n)^2 + (z_0 + z_n)^2}.$$

(6)

Image model In this work, the Image Model is also implemented, which is a generalization of the Loyd-Mirror phenomena with four paths. Fig. 2.2.5 shows the paths which consist of 1) the direct path (R_1), 2) a path with one reflection from the sea surface (R_3), 3) a path with one reflection from the sea bed (R_2), and 4) a path with one reflection from the sea surface, and one reflection from the sea bed (R_4).

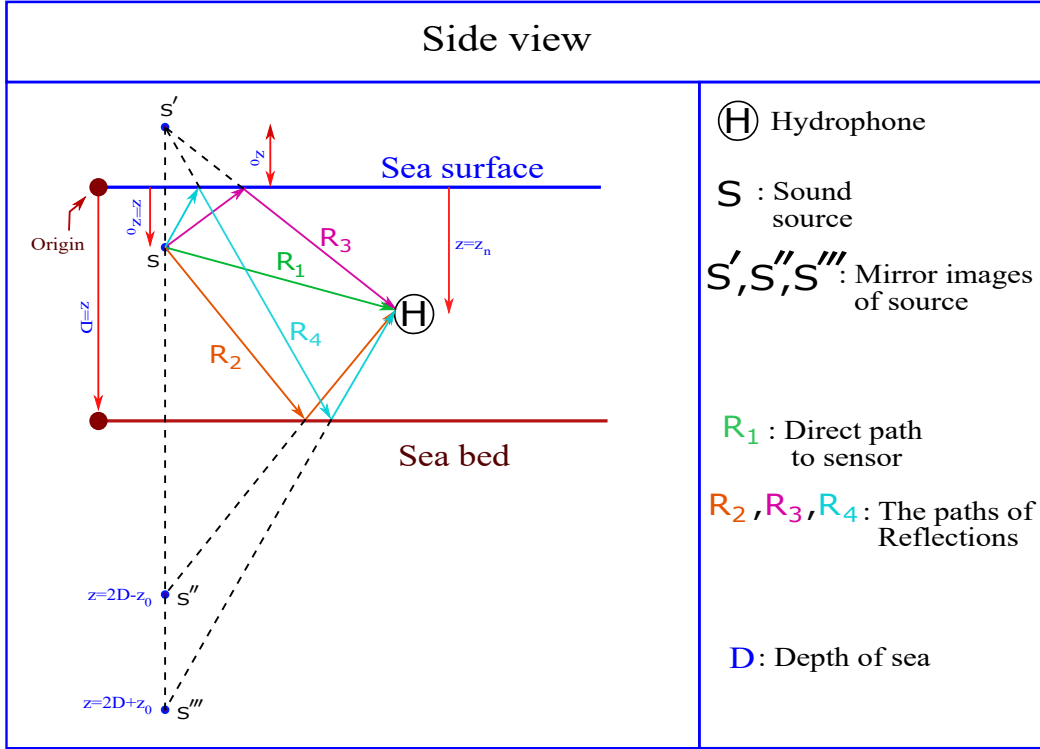


Fig. 2.2.5: Schematic of the Image model.

Using the Image propagation model, the relationship between the source signal $S(\omega)$ and the received signal $H_n(\omega)$ at the n^{th} hydrophone at the angular frequency ω is defined as [2]

$$H_n(\omega) = S(\omega) \times G(p_0, p_n, \omega) = -\frac{S(\omega)}{4\pi} \times \left(\frac{e^{-ikr_{1,n}}}{r_{1,n}} - \frac{e^{-ikr_{2,n}}}{r_{2,n}} - \frac{e^{-ikr_{3,n}}}{r_{3,n}} + \frac{e^{-ikr_{4,n}}}{r_{4,n}} \right), \quad (7)$$

where

$$r_{j,n} = \sqrt{(x_0 - x_n)^2 + (y_0 - y_n)^2 + z_{j,n}^2}, \quad j = 1, \dots, 4,$$

and

$$\begin{aligned} z_1 &= -z_0 + z_n; & z_2 &= 2D - z_0 - z_n; \\ z_3 &= +z_0 + z_n; & z_4 &= 2D + z_0 - z_n. \end{aligned} \quad (8)$$

There are four paths in each mode of the Image model.

Normal-modes model The first three models were based on the ray theory. But, the Normal-modes model is one of the solutions of the following wave equation [2].

$$\rho \nabla \cdot \left(\frac{1}{\rho} \nabla p \right) - \frac{1}{c^2} \frac{\partial^2 p}{\partial t^2} = 0, \quad (9)$$

where p , ρ , ∇ , and ∂ are the acoustic pressure, the density of environment, the divergence operator and the derivative operator, respectively.

The isovelocity problem is one of the problems that is used in the current work. This problem leads to the normal modes solution as follows.

$$H_n(\omega) = S(\omega) \times G(p_0, p_n, \omega) = S(\omega) \times \frac{-i}{\rho(z_0) \sqrt{8\pi r_n}} e^{i\pi/4} \sum_{m=1}^{\infty} \left(\Psi_m(z_0) \Psi_m(z_n) \frac{e^{-ik_{rm}r_n}}{\sqrt{k_{rm}}} \right), \quad (10)$$

where m , $\rho(z_0)$ and k_{rm} are the mode number, the density of water at the depth of source and the horizontal wave number, respectively. Also,

$$\begin{aligned} k_{rm} &= \sqrt{\left(\frac{\omega}{c}\right)^2 - k_{zm}^2}, & k_{zm} &= \left(m - \frac{1}{2}\right) \frac{\pi}{D}, \\ r_n &= \sqrt{(x_0 - x_n)^2 + (y_0 - y_n)^2}, & \Psi_m(z) &= \sqrt{\frac{2\rho}{D}} \sin(k_{zm}z), \end{aligned} \quad (11)$$

where k_{zm} is the vertical wave number.

The maximum number of modes is not necessarily infinity. The modes which cause k_{rm} to be a real number would be taken into account. Thus the maximum number of modes for the frequency f is determined as follows.

$$M < \frac{2fD}{c} + \frac{1}{2}. \quad (12)$$

2.3 Frequency-Domain Localization Algorithms

In this section, different frequency domain estimators will be described. Specifically, in Section 2.3.1, the MUSIC algorithm is described; then, in Section ??, the Mean Square Error (MSE) algorithm is described; and finally, in Section 2.3.2, the Bartlett estimation algorithm is described.

2.3.1 MUSIC localization method

The MUSIC localization method is implemented as described by the following steps [1]

1. Using $R_n(\omega_i)$, the measured signal at the n^{th} hydrophone at angular frequency ω_i in the frequency domain, calculate the eigenvalues and the right eigenvectors of $\bar{\mathbf{R}}(\omega_i)\bar{\mathbf{R}}^{\text{H}}(\omega_i)$ for the i^{th} frequency, where $(\cdot)^{\text{H}}$ is the Hermitian operator, and for an array with N elements, $\bar{\mathbf{R}}(\omega_i)$ is defined as

$$\bar{\mathbf{R}}(\omega_i) = [R_1(\omega_i) \ R_2(\omega_i) \ \dots \ R_N(\omega_i)]^{\text{T}}, \quad (13)$$

where $(\cdot)^{\text{T}}$ is the transpose operator. Note that by definition λ is the eigenvalue of the matrix \mathbf{A} , if $\det(\lambda\mathbf{I} - \mathbf{A}) = 0$, where \mathbf{I} is the identity matrix with the proper dimensions, and $\det(\lambda\mathbf{I} - \mathbf{A})$ is the determinant of the matrix $\lambda\mathbf{I} - \mathbf{A}$. If the vector \mathbf{V} is the corresponding right eigenvector of the eigenvalue λ , then it can be obtained using $\mathbf{A}\mathbf{V} = \lambda\mathbf{V}$. For a square matrix with dimension $K \times K$, the number of eigenvalues and eigenvectors is equal to K . The dimension of each eigenvector is $K \times 1$. As such, the matrix of eigenvectors can be represented as

$$\bar{\mathbf{V}} = [\mathbf{V}_1 \ \mathbf{V}_2 \ \dots \ \mathbf{V}_{K-1} \ \mathbf{V}_K] = \begin{bmatrix} v_{11} & \dots & v_{1K} \\ \vdots & \dots & \vdots \\ v_{K1} & \dots & v_{KK} \end{bmatrix}_{K \times K}. \quad (14)$$

The vectors $\mathbf{V}_1, \mathbf{V}_2, \dots, \mathbf{V}_K$ are the K right eigenvectors corresponding to the N eigenvalues.

2. Next, sort the calculated eigenvalues based on the absolute values of their real parts in descending order, and then sorting the corresponding eigenvectors as the order of the sorted eigenvalues. We call them $\mathbf{V}_s(\omega_i)$. This process is done for each angular frequency ω_i .
3. Eliminate the first eigenvector and obtain the matrix of remaining eigenvectors as

$$\bar{\mathbf{V}}_s(\omega_i) = [\mathbf{V}_{s2}(\omega_i) \ \mathbf{V}_{s3}(\omega_i) \ \dots \ \mathbf{V}_{sN-1}(\omega_i) \ \mathbf{V}_{sN}(\omega_i)]. \quad (15)$$

This process is done for each angular frequency ω_i .

4. The estimated location of source $\hat{p}_0 = (\hat{x}_0, \hat{y}_0, \hat{z}_0)$ is obtained as

$$\hat{p}_0 = \arg \max_p \left\{ \left(\sum_i \left(\sum_{n=2}^N |\mathbf{V}_{s_n}^H(\omega_i) \cdot \bar{\mathbf{G}}(p, \omega_i)|^2 \right)^{-0.5} \right) \right\}, \quad (16)$$

where $\mathbf{V}_{s_n}^H(\omega_i)$ is the Hermitian of \mathbf{V}_{s_n} at the angular frequency ω_i . Also

$$\bar{\mathbf{G}}(p, \omega_i) = \left[\frac{G(p, p_1, \omega_i)}{|G(p, p_1, \omega_i)|} \quad \frac{G(p, p_2, \omega_i)}{|G(p, p_2, \omega_i)|} \quad \dots \quad \frac{G(p, p_N, \omega_i)}{|G(p, p_N, \omega_i)|} \right]^\top, \quad (17)$$

where $|\cdot|$ denotes the absolute value of its argument, and $G(p, p_n, \omega_i)$ is the equation of the chosen propagation model. Thus, $G(p, p_n, \omega_i)$ is chosen from one of the equations (2) or (5) or (7) or (10).

2.3.2 MSE localization method

The mean squared error (MSE) localization method estimates the location of source $\hat{p}_0 = (\hat{x}_0, \hat{y}_0, \hat{z}_0)$ as follows.

$$\hat{p}_0 = \arg \min_p \left\{ \left(\sum_i \left(\sum_{\eta=1}^N \sum_{n=\eta+1}^N |\Gamma_{\eta n}(p, \omega_i)|^2 \right)^{-0.5} \right) \right\}, \quad (18)$$

where

$$\Gamma_{\eta n}(p, \omega_i) = \frac{G(p, p_\eta, \omega_i) G^H(p, p_n, \omega_i)}{|G(p, p_\eta, \omega_i) G^H(p, p_n, \omega_i)|} - \frac{R_\eta(\omega_i) R_n^H(\omega_i)}{|R_\eta(\omega_i) R_n^H(\omega_i)|}. \quad (19)$$

where $G(p, p_1, \omega_i)$ and $R_n(\omega_i)$ are the equation of the chosen propagation model and the measured signal at the n^{th} hydrophone, respectively.

2.3.3 Bartlett localization method

The Bartlett localization method estimates the location of source $\hat{p}_0 = (\hat{x}_0, \hat{y}_0, \hat{z}_0)$ as follows [1].

$$\hat{p}_0 = \arg \max_p \left\{ \left(\sum_i \left(\frac{\bar{\mathbf{G}}(p, \omega_i) \bar{\mathbf{R}}^H(\omega_i) \bar{\mathbf{R}}(\omega_i) \bar{\mathbf{G}}^H(p, \omega_i)}{|\bar{\mathbf{G}}(p, \omega_i) \bar{\mathbf{G}}^H(p, \omega_i)|} \right)^1 \right) \right\}, \quad (20)$$

where

$$\begin{aligned} \bar{\mathbf{G}}(p, \omega_i) &= [G(p, p_1, \omega_i) \quad G(p, p_2, \omega_i) \quad \dots \quad G(p, p_N, \omega_i)], \\ \bar{\mathbf{R}}(\omega_i) &= [R_1(\omega_i) \quad R_2(\omega_i) \quad \dots \quad R_N(\omega_i)]. \end{aligned} \quad (21)$$

$G(p, p_1, \omega_i)$ and $R_n(\omega_i)$ are the equation of the chosen propagation model and the measured signal at the n^{th} hydrophone, respectively.

2.4 Time-Domain Localization Algorithms

In this section, the time-domain localization methods MUSIC and MCCC are explained.

2.4.1 MCCC localization method

MCCC is a time-domain approach to estimate the time delay of arrival (TDOA) in free space when the hydrophone (or microphone) array has more than two elements [1]. Assume that $s(t_k)$ is the time value of a given acoustic source at time t_k , and is located at the point $p_0 = (x_0, y_0, z_0)$ (in the Cartesian coordinate system). This value is received at the n^{th} hydrophone with the location $p_n = (x_n, y_n, z_n)$ at the time $t_k + \tau_n$. Thus, for a hydrophone array with N elements in a noiseless free space, the received signal at the n^{th} element at time t is calculated as

$$h_n(t) = g(s(t), p_0, p_n) = \alpha(p_0, p_n)s(t - \tau_n(p_0)), \quad (22)$$

where $\alpha(p_0, p_n)$ is the loss, $\alpha(p_0, p_n) \in \{\mathbb{R} | 0 \leq \alpha(p_0, p_n) \leq 1\}$. Also,

$$\tau_n(p_0) = \frac{\sqrt{(x_0 - x_n)^2 + (y_0 - y_n)^2 + (z_0 - z_n)^2}}{c},$$

where c is the sound speed. One can represent (22) as

$$s(t) = g^{-1}(h_n(t), p_0, p_n) = \frac{h_n(t + \tau_n(p_0))}{\alpha(p_0, p_n)}. \quad (23)$$

Using the measured signals $h_n(t_k)$, $n = 1, 2, \dots, N$ at discrete time $t_k = t_{\min} + k \Delta t$, where Δt is the sampling time, and $k = 0, 1, \dots, L - 1$, where $L \in \mathbb{N}$, the discrete-time transmit signal at position \tilde{p}_0 can be expressed as

$$s_n(t_k, \tilde{p}_0) \triangleq g^{-1}(h_n(t_k), \tilde{p}_0, p_n) = \frac{h_n(t_k + \tau_n(\tilde{p}_0))}{\alpha(\tilde{p}_0, p_n)}, \quad (24)$$

One can conclude from (23) and (24) that if the point $\tilde{p}_0 = (\tilde{x}_0, \tilde{y}_0, \tilde{z}_0)$ is the correct location of the source then all N values $s_n(t_k, \tilde{p}_0)$, $n = 1, 2, \dots, N$ are almost completely correlated with each other at the time t_k . As such, using the MCCC method, the correlation measurement criterion and thus the source location is defined based on the determinant of the cross-correlation matrix $\mathbf{C}_c(p)$, calculated by [1]

$$\hat{p}_0 = \arg \min_p \left\{ \det [\mathbf{C}_c(p)] \right\}, \quad (25)$$

where $\hat{p}_0 = (\hat{x}_0, \hat{y}_0, \hat{z}_0)$ is the estimated location of the source. The matrix $\mathbf{C}_c(p)$ for each point $p = (x, y, z)$ of the search space $\mathbb{R}^{3 \times Q}$ is obtained as (the search space contains Q 3-dimensional points)

$$\mathbf{C}_c(p) = \frac{\mathbf{C}(p) \mathbf{C}^\top(p)}{L}, \quad (26)$$

where $(\cdot)^\top$ is the transpose operator. Also,

$$\mathbf{C}(p) = \begin{bmatrix} h_1(t_0 + \tau_1(p)) & \dots & h_1(t_{L-1} + \tau_1(p)) \\ h_2(t_0 + \tau_2(p)) & \dots & h_2(t_{L-1} + \tau_2(p)) \\ \vdots & \ddots & \vdots \\ h_N(t_0 + \tau_N(p)) & \dots & h_N(t_{L-1} + \tau_N(p)) \end{bmatrix}. \quad (27)$$

According to (27), one can also write (26) as

$$\mathbf{C}_c(p) = \frac{1}{L} \sum_{k=0}^{L-1} (\bar{\mathbf{s}}^\top(t_k, p) \bar{\mathbf{s}}(t_k, p)), \quad (28)$$

where $\bar{\mathbf{s}}(t_k, p) = [h_1(t_k + \tau_1(p)), \dots, h_N(t_k + \tau_N(p))]$.

According to (23), $h_n(t_k + \tau_n(p))$ is equal to $s_n(t_k, p)$ for $n = 1, 2, \dots, N$. Note that the MCCC method uses $s_n(t_k, p)$ but does not need to have a measure of the loss to calculate the cross-correlation matrix.

The spatial correlation matrix $\mathbf{C}_c(p)$ can be written as [1]

$$\mathbf{C}_c(p) = \begin{bmatrix} \sigma_1^2 & \Gamma_{12} & \dots & \Gamma_{1N} \\ \Gamma_{21} & \sigma_2^2 & \dots & \Gamma_{2N} \\ \vdots & \vdots & \ddots & \vdots \\ \Gamma_{N1} & \Gamma_{N2} & \dots & \sigma_N^2 \end{bmatrix} \quad (29)$$

In [1], it has been shown that $\mathbf{C}_c(p)$ in 25 can be replaced by the following cross-correlation matrix.

$$\tilde{\mathbf{C}}_c(p) = \begin{bmatrix} 1 & \frac{\Gamma_{12}}{\sigma_1 \times \sigma_2} & \dots & \frac{\Gamma_{1N}}{\sigma_1 \times \sigma_N} \\ \frac{\Gamma_{21}}{\sigma_2 \times \sigma_1} & 1 & \dots & \frac{\Gamma_{2N}}{\sigma_2 \times \sigma_N} \\ \vdots & \vdots & \ddots & \vdots \\ \frac{\Gamma_{N1}}{\sigma_N \times \sigma_1} & \frac{\Gamma_{N2}}{\sigma_N \times \sigma_2} & \dots & 1 \end{bmatrix}. \quad (30)$$

2.4.2 MUSIC Estimator

The MUSIC localization method in the time-domain is implemented as described in the following steps [1].

1. Calculating the eigenvalues and the right eigenvectors of the time-domain cross-correlation matrix $\mathbf{C}_c(p)$, where $\mathbf{C}_c(p)$ is obtained from (24).
2. Sorting the calculated eigenvalues based on the absolute values of their real parts in descending order, and then sorting the corresponding eigenvectors as the order of the sorted eigenvalues. They are defined as $\mathbf{V}_s(p)$.

3. Eliminating the first eigenvector and obtaining the matrix of remaining eigenvectors as follows.

$$\bar{\mathbf{V}}_s(p) = [\mathbf{V}_{s2}(p) \ \mathbf{V}_{s3}(p) \ \cdots \ \mathbf{V}_{sN-1}(p) \ \mathbf{V}_{sN}(p)]. \quad (31)$$

4. The estimated location of source $\hat{p}_0 = (\hat{x}_0, \hat{y}_0, \hat{z}_0)$ is obtained as follows.

$$\hat{p}_0 = \arg \max_p \left\{ \left(\sum_{n=2}^N \left(\mathbf{V}_{sn}^\top(p) \cdot \mathbf{C}_c(p) \cdot \mathbf{V}_{sn}(p) \right) \right)^{-1} \right\}. \quad (32)$$

2.5 Proposed Algorithm for High Frequency Localization

As mentioned in the previous section, MCCC has good resolution, but it cannot distinguish sources present in different frequency bands, because it is a time-domain method. In the proposed algorithm, a time-domain cross-correlation matrix which contains the information of specific frequency band is calculated using an approximation on the inverse fast Fourier transform (IFFT). Then, the approximate cross-correlation matrix is used in a form of 25 to find the location of the source. The proposed method, in addition to taking advantages of both time- and frequency-domain methods, also takes into account the features of the propagation model of environment. This is a very important feature particularly in a shallow water environment, in which the received signal arrives at the receiver through multiple paths. Thus, using a propagation model that takes into account other paths in addition to the direct path is very useful in the underwater localization.

The proposed method can be used with different propagation models such as Lloyd-Mirror, Image, and Normal-modes. Considering the propagation models defined for the different propagation models, one can represent the received signal in the frequency domain as

$$S(\omega) = H_n(\omega) \times G^{-1}(p_0, p_n, \omega). \quad (33)$$

Considering that $H_n(\omega_l)$ states the l^{th} frequency component of the FFT of the measured time signal $h_n(t_k)$, $k = 0, 1, \dots, L - 1$, where $t_k = t_{\min} + k \Delta t$. Δt is the sampling time. Also, the discretized frequency samples are equal to [2]

$$\omega_l = l \Delta \omega, \quad l = 0, 1, \dots, \lfloor \frac{L}{2} - 1 \rfloor, \quad \Delta t \Delta \omega = \frac{2\pi}{L}, \quad (34)$$

where $\lfloor \cdot \rfloor$ denotes the floor value of its argument.

Defining $S_n(\omega_l, p) \triangleq H_n(\omega_l) \times G^{-1}(p, p_n, \omega_l)$, the cross-correlation matrix for the MCCC method is calculated using (28) and

$$\begin{aligned} \bar{\mathbf{s}}(t_k, p) &= F^{-1}[\bar{\mathbf{S}}(\omega, p)], \\ \bar{\mathbf{S}}(\omega, p) &= \left[\frac{H_1(\omega)|G(p, p_1, \omega)|}{G(p, p_1, \omega)} \cdots \frac{H_N(\omega)|G(p, p_N, \omega)|}{G(p, p_N, \omega)} \right], \end{aligned} \quad (35)$$

where $F^{-1}[\cdot]$ stands for the IFFT. Also, $|\cdot|$ denotes the absolute value of its argument.

The IFFT of $\bar{\mathbf{S}}(\omega, p)$ is defined as [2]

$$\bar{\mathbf{s}}(t_k, p) = \frac{\Delta \omega}{2\pi} \text{Re} \left\{ \sum_{l=0}^{\frac{L}{2}-1} \left(\epsilon_l \bar{\mathbf{S}}(\omega_l, p) e^{-i\omega_l t_{\min}} e^{-i\frac{2\pi l k}{L}} \right) \right\}, \quad (36)$$

where $\text{Re}\{\cdot\}$ denotes the real part of its argument. Also $\epsilon_0 = 1$, and $\epsilon_l = 2$ for $l > 0$. One can represent (36) as

$$\bar{\mathbf{s}}(t_k, p) = \sum_{l=0}^{\frac{L}{2}-1} \left([\text{Re}\{\mathbf{T}_1(l, p)\}] (\text{Re}\{T_2(l, k)\}) - [\text{Im}\{\mathbf{T}_1(l, p)\}] (\text{Im}\{T_2(l, k)\}) \right), \quad (37)$$

where $\text{Im}\{\cdot\}$ denotes the imaginary part of its argument, and

$$\begin{cases} \mathbf{T}_1(l, p) = \frac{\Delta\omega}{2\pi} \epsilon_l \bar{\mathbf{S}}(\omega_l, p) e^{-i\omega_l t_{\min}}, \\ T_2(l, k) = e^{-i\frac{2\pi lk}{L}}. \end{cases} \quad (38)$$

By calculating (37) in a specific frequency range (by considering specific values of $l \in \{0, 1, \dots, (L/2) - 1\}$ that are corresponding to the chosen frequencies), and then substituting the result in (28), the frequency limited time-domain cross-correlation matrix is obtained. Assuming that each frequency component is weakly correlated with the other frequency components, by substituting (37) in (28) and ignoring the uncorrelated terms, the proposed cross-correlation matrix is approximated as follows.

$$\begin{aligned} \mathbf{C}_c(p) \approx & \frac{1}{L} \sum_{l_f} \left(\left[[\text{Re}\{\mathbf{T}_1(l_f, p)\}]^\top [\text{Re}\{\mathbf{T}_1(l_f, p)\}] \right] \times \left(\sum_{k=0}^{L-1} (\text{Re}\{T_2(l_f, k)\})^2 \right) \right. \\ & - \left[[\text{Re}\{\mathbf{T}_1(l_f, p)\}]^\top [\text{Im}\{\mathbf{T}_1(l_f, p)\}] + [\text{Im}\{\mathbf{T}_1(l_f, p)\}]^\top [\text{Re}\{\mathbf{T}_1(l_f, p)\}] \right] \times \\ & \left(\sum_{k=0}^{L-1} (\text{Re}\{T_2(l_f, k)\} \text{Im}\{T_2(l_f, k)\}) \right) + \left[[\text{Im}\{\mathbf{T}_1(l_f, p)\}]^\top [\text{Im}\{\mathbf{T}_1(l_f, p)\}] \right] \times \\ & \left. \left(\sum_{k=0}^{L-1} (\text{Im}\{T_2(l_f, k)\})^2 \right) \right), \end{aligned} \quad (39)$$

where l_f is a set that only contains chosen frequency indices, and according to the chosen frequency range is a subset from the set $\{0, 1, \dots, (L/2) - 1\}$. The speed of calculations in this approximation is acceptable, because the term T_2 which is scalar is independent of signal $\bar{\mathbf{S}}(\omega_l, p)$, and thus the calculations in each time sample do not include the matrix values and matrix operations. In the other words, if the number of chosen frequencies is α , then in the case with the approximation there only would be α matrix operations, but in the case without the approximation there would be $L \times \alpha$ matrix operations.

To better understand the proposed method, consider the following equation that is obtained by substituting (37) in (28).

$$\begin{aligned} \mathbf{C}_c(p) = & \frac{1}{L} \sum_{k=0}^{L-1} (\bar{\mathbf{s}}^\top(t_k, p) \cdot \bar{\mathbf{s}}(t_k, p)) = \frac{1}{L} \sum_{k=0}^{L-1} \left(\left(\sum_{l=0}^{\frac{L}{2}-1} ([\text{Re}\{\mathbf{T}_1(l, p)\}]^\top (\text{Re}\{T_2(l, k)\})) \right) - \right. \\ & \left. \sum_{l=0}^{\frac{L}{2}-1} ([\text{Im}\{\mathbf{T}_1(l, p)\}]^\top (\text{Im}\{T_2(l, k)\})) \right) \cdot \left(\sum_{l=0}^{\frac{L}{2}-1} ([\text{Re}\{\mathbf{T}_1(l, p)\}] (\text{Re}\{T_2(l, k)\})) - \right. \\ & \left. \sum_{l=0}^{\frac{L}{2}-1} ([\text{Im}\{\mathbf{T}_1(l, p)\}] (\text{Im}\{T_2(l, k)\})) \right). \end{aligned}$$

Therefore, there are four multiplications. To avoid congestion, the first multiplication is expanded. The other three multiplications are expanded in the similar manner. The first multiplication is expanded such that

$$\mathbf{M}_1(p) = \frac{1}{L} \sum_{k=0}^{L-1} \left(\left(\sum_{l=0}^{\frac{L}{2}-1} ([\text{Re}\{\mathbf{T}_1(l, p)\}]^\top (\text{Re}\{T_2(l, k)\})) \right) \cdot \left(\sum_{l=0}^{\frac{L}{2}-1} ([\text{Re}\{\mathbf{T}_1(l, p)\}] (\text{Re}\{T_2(l, k)\})) \right) \right),$$

where k and l are the indices of time and frequency, respectively. $\mathbf{M}_1(p)$ presents a summation over time of the multiplication of two terms. Let's define the two terms to be $\mathbf{T}\mathbf{r}_1$ and $\mathbf{T}\mathbf{r}_2$. Then,

$$\begin{aligned} \mathbf{T}\mathbf{r}_1 &= \left(\sum_{l=0}^{\frac{L}{2}-1} ([\text{Re}\{\mathbf{T}_1(l, p)\}]^\top (\text{Re}\{T_2(l, k)\})) \right), \\ \mathbf{T}\mathbf{r}_2 &= \left(\sum_{l=0}^{\frac{L}{2}-1} ([\text{Re}\{\mathbf{T}_1(l, p)\}] (\text{Re}\{T_2(l, k)\})) \right). \end{aligned}$$

Note that $\mathbf{T}\mathbf{r}_1$ and $\mathbf{T}\mathbf{r}_2$ are a summation of the frequency components from frequency index $l = 0$ to frequency index $l = \frac{L}{2} - 1$. A specific frequency index corresponds to a specific frequency. We suppose that the frequency components of $\mathbf{T}\mathbf{r}_1$ and $\mathbf{T}\mathbf{r}_2$ are correlated with each other if they have the same indices. For example, the 0th frequency component of $\mathbf{T}\mathbf{r}_1$ (i.e. the component with the index $l = 0$) is only correlated with the 0th frequency component of $\mathbf{T}\mathbf{r}_2$. Therefore, the 0th frequency component of $\mathbf{T}\mathbf{r}_1$ is not correlated with the 1st frequency component of $\mathbf{T}\mathbf{r}_2$. Thus, based on this assumption a component of $\mathbf{T}\mathbf{r}_1$ is correlated with a component of $\mathbf{T}\mathbf{r}_2$ if the two components correspond to the same frequency, otherwise they are uncorrelated. Given this assumption, we ignore the uncorrelated terms in the multiplication of $\mathbf{T}\mathbf{r}_1$ and $\mathbf{T}\mathbf{r}_2$. Therefore, $\mathbf{M}_1(p)$ is simplified as follows.

$$\begin{aligned} \mathbf{M}_1(p) &\approx \frac{1}{L} \sum_{k=0}^{L-1} \left(\sum_{l=0}^{\frac{L}{2}-1} \left([\text{Re}\{\mathbf{T}_1(l, p)\}]^\top (\text{Re}\{T_2(l, k)\}) [\text{Re}\{\mathbf{T}_1(l, p)\}] (\text{Re}\{T_2(l, k)\}) \right) \right) = \\ &\frac{1}{L} \sum_{k=0}^{L-1} \left(\sum_{l=0}^{\frac{L}{2}-1} \left(\left[[\text{Re}\{\mathbf{T}_1(l, p)\}]^\top [\text{Re}\{\mathbf{T}_1(l, p)\}] \right] \times (\text{Re}\{T_2(l, k)\})^2 \right) \right). \end{aligned}$$

It should be noted that $\mathbf{T}_1(l, p)$ is a vector while $T_2(l, k)$ is a scalar. It is obvious that the two summations can be replaced with each other. Hence,

$$\mathbf{M}_1(p) \approx \frac{1}{L} \sum_{l=0}^{\frac{L}{2}-1} \left(\sum_{k=0}^{L-1} \left(\left[[\text{Re}\{\mathbf{T}_1(l, p)\}]^\top [\text{Re}\{\mathbf{T}_1(l, p)\}] \right] \times (\text{Re}\{T_2(l, k)\})^2 \right) \right).$$

Since $\left[[\text{Re}\{\mathbf{T}_1(l, p)\}]^\top [\text{Re}\{\mathbf{T}_1(l, p)\}] \right]$ is not related to time k , it can come out from the second summation, and can be expressed as

$$\mathbf{M}_1(p) \approx \frac{1}{L} \sum_{l=0}^{\frac{L}{2}-1} \left(\left[\text{Re} \{ \mathbf{T}_1(l, p) \} \right]^\top \left[\text{Re} \{ \mathbf{T}_1(l, p) \} \right] \times \left(\sum_{k=0}^{L-1} (\text{Re} \{ T_2(l, k) \})^2 \right) \right).$$

As such, the first term of (37) is obtained from this expression. The other three terms are obtained in the similar manner.

To increase the resolution, an implementation of the criterion (25) is used in the proposed algorithm and can be expressed as

$$\hat{p}_0 = \arg \min_p \left\{ \left(\det [\mathbf{C}_c(p)] \right)^2 \right\}. \quad (40)$$

Finally, by substituting (39) in (40), the location of source is estimated using the proposed algorithm.

2.6 Evaluation of the Performance

2.6.1 Sea Trials

A sea trial experiment took place between August 14, 2019 and August 21, 2019 in Grand Passage, Nova Scotia. A variety of signals were transmitted underwater via acoustics, and then the receiver was left to sense and record for a period of 7 days. A map showing the location of the sensor and two transmit locations is shown in Figure 2.6.1.



Fig. 2.6.1: Map of the area

The final location of the receiver is shown in Table 2. The depth at this location is approximately 20 meters.

Table 2: Location of the receiver and transmitter stations

Sensor	44° 17'28.45" N	66° 20'36.58" W
Tx Station # 1	44° 17'28.79" N	66°20'30.84" W
Tx Station #2	44° 17'33.51" N	66°20'31.04" W

The sensor consisted of:

1. One 5-element hydrophone array shown in Figure 2.6.2. GTI's wideband hydrophones (M5-900) with a sensitivity of -193 dB/ μ V are utilized. The hydrophone array is deployed horizontally and moored to the bottom of the ocean.
2. One waterproof, pressure-resistant, battery-powered case to record and store data from the hydrophone array shown in Figure 2.6.3. The TR-ORCA vessel is manufactured by



Fig. 2.6.2: A 5-element horizontal array

Turbulent Research and all channels are phase and frequency synchronous. The sample rate is 384 kSps. The available memory is 1 TB. A schedule is programmed to allow recording over several days. The schedule is programmed to be recording for twelve hours, followed by a sleep period of 24 hours.

3. A weighted cage to protect the delicate recording equipment. The hydrophones plate is installed a few cm above the rail of the cage.
4. An acoustic release system for retrieval.

Deployment A crane was used to lower the receiver into the research vessel from the government wharf in Freeport, NS. A hoist available on Luna Ocean's vessel was later used to deploy the receiver in the waters in Grand Passage, Nova Scotia, in the Bay of Fundy. A picture during the deployment is shown in Figure 2.6.4. The bearing of the array as it was lowered during the deployment was coarsely estimated to be NE, and a more precise bearing is confirmed by validating the vessel localization output with its true GPS coordinates at different times during the trial.



Fig. 2.6.3: Installation of the hydrophone array and acoustic releases in a frame.



Fig. 2.6.4: Deployment of the receiver using the hoist

Signals of interest

The harbour porpoise The harbour porpoise vocal consists of high-frequency short-time clicks with the center frequency about 135 kHz and bandwidth about 30 kHz. In [10], field recordings of harbour porpoises were made in the inner Danish waters with a vertical array of three or four hydrophones. The back-calculated source level ranged from 178 to 205 dB re $1\mu\text{Pa}$ 1 m with a mean source level of 191 dB re $1\mu\text{Pa}$ 1 m. Calculations based on the sonar equation indicate that harbour porpoises, using these high click intensities, should be capable of detecting fish and nets. Harbour porpoises in this study preferred a relatively constant inter-click interval of about 60 ms, but intervals up to 200 ms and down to 30 ms were also recorded. Examples of echolocation clicks recorded on August 16, at 1:28pm are shown in Figure 2.6.5.

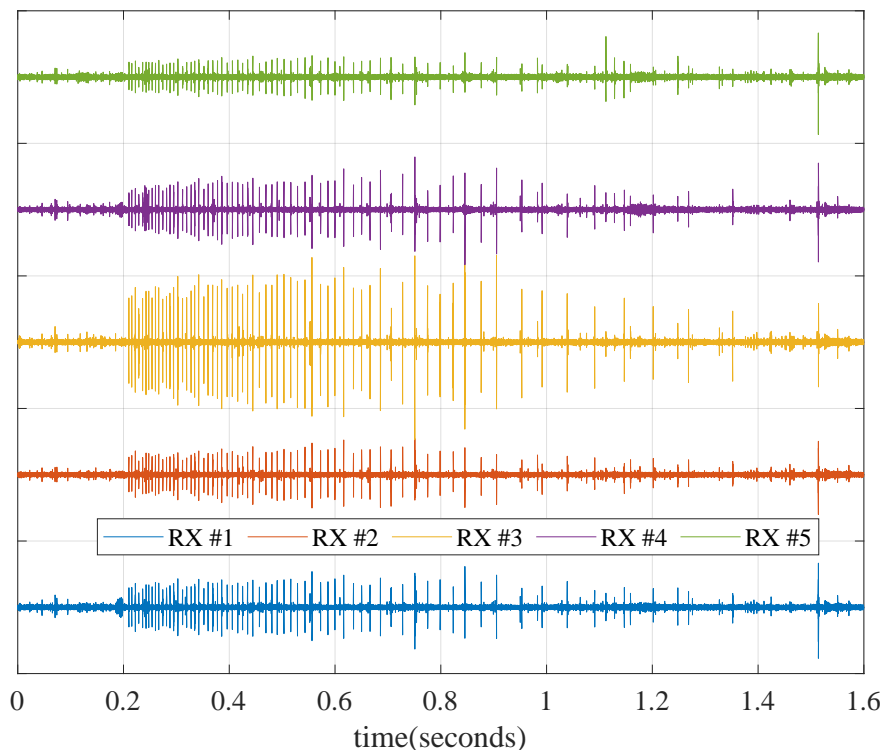
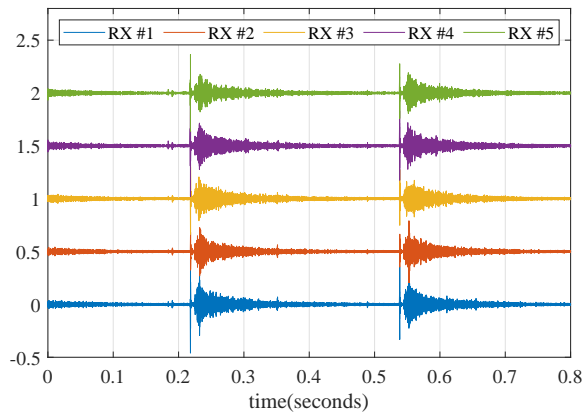


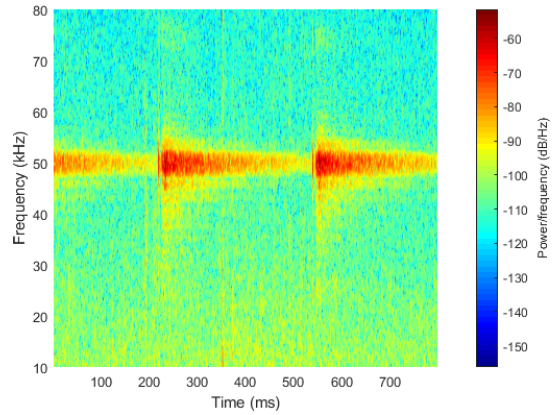
Fig. 2.6.5: In the window between 0.2 and 0.8 seconds, 53 clicks are emitted, with an average click interval of 11 msec. Clicks last on the order of 0.1 msec.

The vessel sonar. Luna Ocean's vessel captained by Greg Trowse had a sonar activated during deployment, and between transmit stations. The primary tone was transmitted periodically near 47 kHz. A representation of the sonar pulse is shown in Figure 2.6.6.

Note that the vessel propeller noise was also used to test low frequency localization algorithms. Several vocalizations and echolocations of dolphins and unknown species of whales were also heard during the 7-day trial. Finally, note that during the 7-day trial at periods of high flow, the noise was overwhelming the analog front-end circuit putting them into saturation. The data had to be discarded in those circumstances.



(a) Sonar pulse waveform from the five sensors. Note that each channel is offset for easier visualisation.



(b) Spectrogram for the first channel.

Fig. 2.6.6: Sonar Waveform and Spectrogram.

2.6.2 Estimation of bearing and range

In this section, the localization algorithms are tested using data from the sea trials. The Bartlett algorithm and the proposed localization methods are compared to locate high frequency sources. At the time of the report, the localization algorithms were analyzed for the sonar pulse, and similar algorithms will be documented for the harbour porpoise in the next report.

Figs. 2.2.1 and 2.2.2 that were presented in Section 2.2.1 show the geometry and placement of the hydrophone array within the coordinate system. The used hydrophone array is a planar array and contains five hydrophones. It was mounted near the sea bed at a depth of approximately 19.3 m, in the Grand Passage, Nova Scotia, Canada. The first hydrophone is at the center of array and its location is $(x_1, y_1, z_1) = (0, 0, 19.3 \text{ m})$. The other four hydrophones are located at the corners of a horizontal square with the side length of 22.9 cm and the center location of $(0, 0, 19.3 \text{ m})$. The depth of sea is about 20 m, and the sound speed is considered as 1495 m/s. The data was recorded in August 2019 with the sample rate of 384 kHz.

Fig. 2.6.7 shows the received signals of the 50 kHz sonar signal at five hydrophones at 12:08pm. At this time, the vessel did a loop near the Sensor Array, and then headed towards the Tx Station #1, where it was anchored at approximately 12:15pm. The time delay between the signals of the hydrophones is clearly visible.

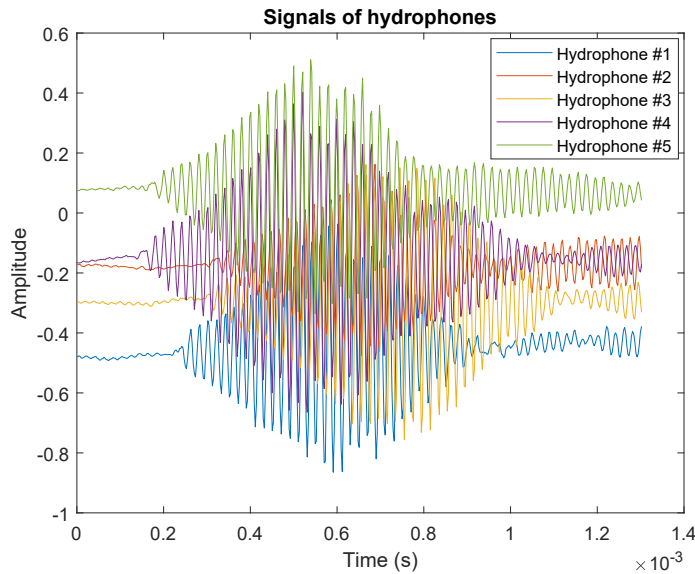
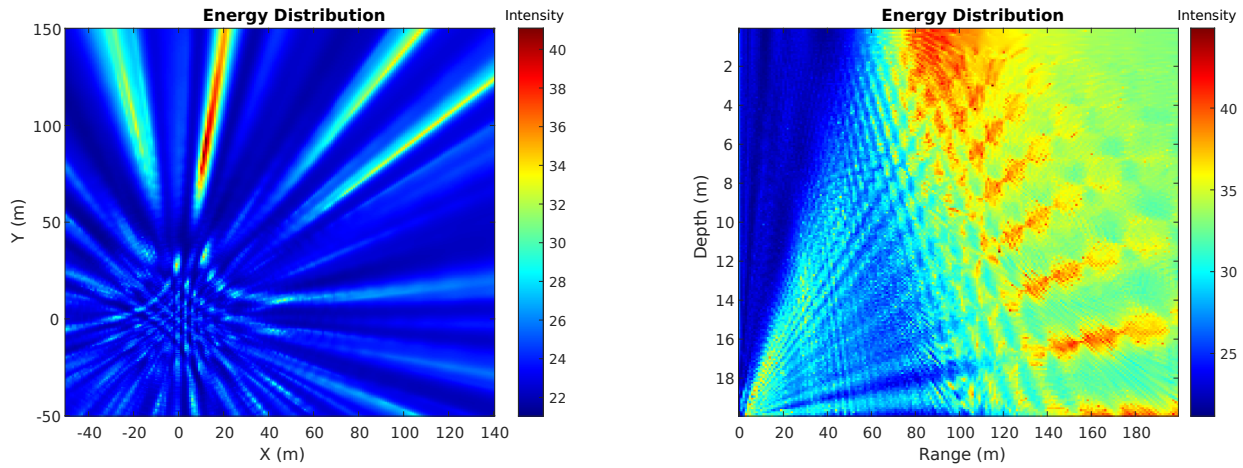


Fig. 2.6.7: Received signals of a sonar at the five hydrophones.

The localization algorithm of the sonar was tested over a three-dimensional space. Fig 2.6.8a represents the calculated energy of a hypothetical source (or the ambiguity figure) at the depth of 0.7 m on the plane view. Next, by sweeping the area around the maximum energy using the RBD coordinate system, the bearing of the maximum energy was obtained to be approximately 82.5 deg. Fig 2.6.8b represents the ambiguity figure at the bearing of 82.5 deg in each grid of range and depth. Note that the MSE estimator with the Image propagation model are used to obtain this results.

The boat was localized using the sonar with the proposed method when the boat was at the two transmit stations, and a comparison between the true GPS location and the estimated value is shown in Table 3. Note that bearing is calculated relative to the Cartesian grid shown in



(a) Plane view, at a depth of 0.7 m.

(b) Elevation view, at a bearing of 82.5 deg.

Fig. 2.6.8: 3D Localization of the sonar pulse using ambiguity function. Regions of high intensity represent potential location of the target.

Figure 2.2.2. While the bearing is accurate, the range estimator can be improved for example, using averaging over multiple sonar pulses.

Table 3: Comparison of estimated position using proposed algorithm with true location.

	From GPS	Estimation
Tx #1	129 \angle 46 $^\circ$	183 \angle 49 $^\circ$
Tx #2	200 \angle 92 $^\circ$	196 \angle 97 $^\circ$

To validate the localization using the sonar, the boat was also localized using the propeller noise. By applying the MSE method with the Lloyd model on the received signals, an area at the depth of 0.7 m was swept for each time step of 1 s. Figs 2.6.9, 2.6.10a and 2.6.10b respectively represent the complete path, the range (the horizontal distance from the origin) and the bearing (azimuth) of the maximum energy calculated using the MSE method with the Lloyd-mirror propagation model over a period of about 270 s.

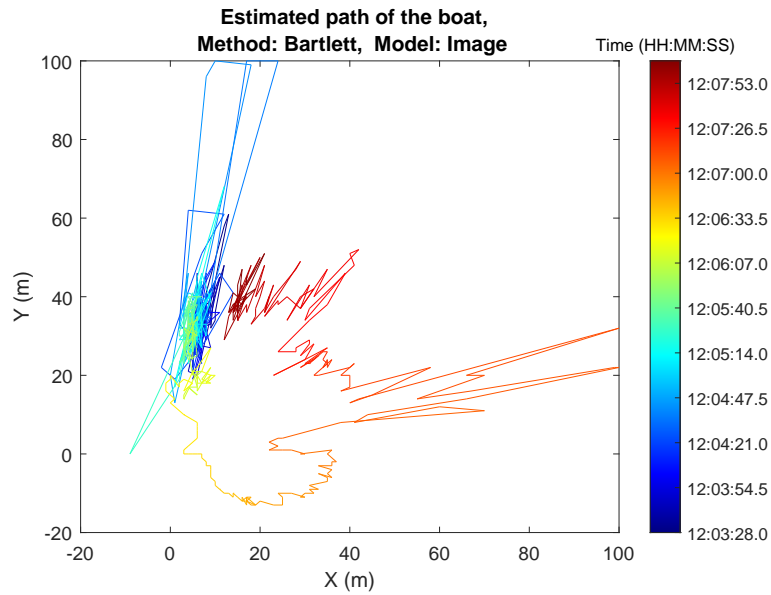
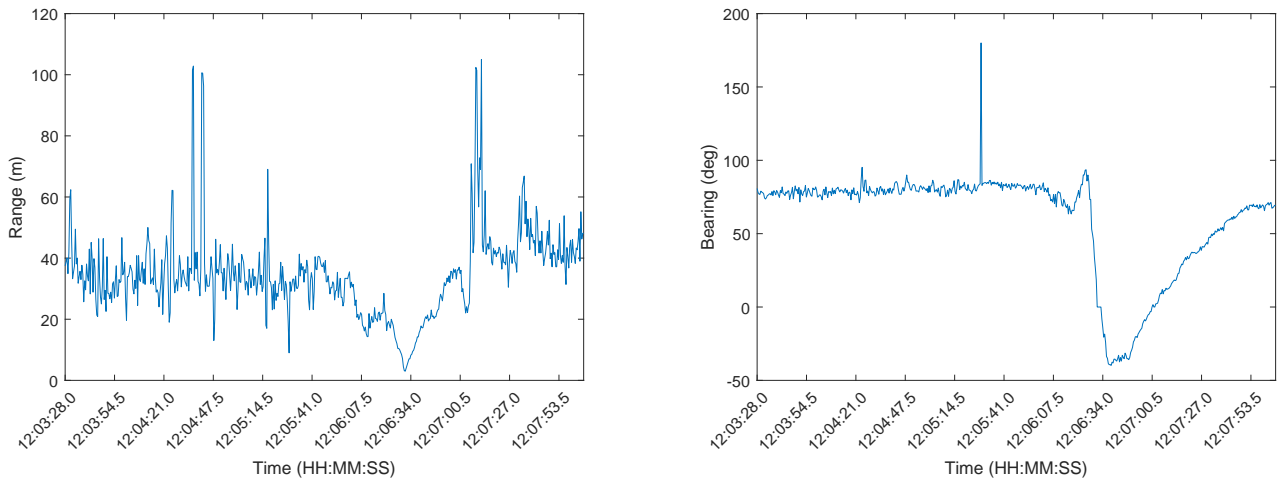


Fig. 2.6.9: The complete path of the maximum energy for the propeller noise of the boat.



(a) The range (distance from the origin).

(b) The bearing (azimuth) of the vessel.

Fig. 2.6.10: Localization using vessel propeller noise

Next, we analyze the echo-location of a harbour porpoise, recorded at approximately 12:40pm, on August 14, 2019. Note that in the logbook prepared by the students, harbour porpoises had been observed at 12:42pm. Fig. 2.6.11 shows the recorded signal of harbour porpoise vocalizations over a 20 second period accompanied with a zoomed in version that shows a first pulse followed by potential multipath arrivals due to bottom or surface bounce.

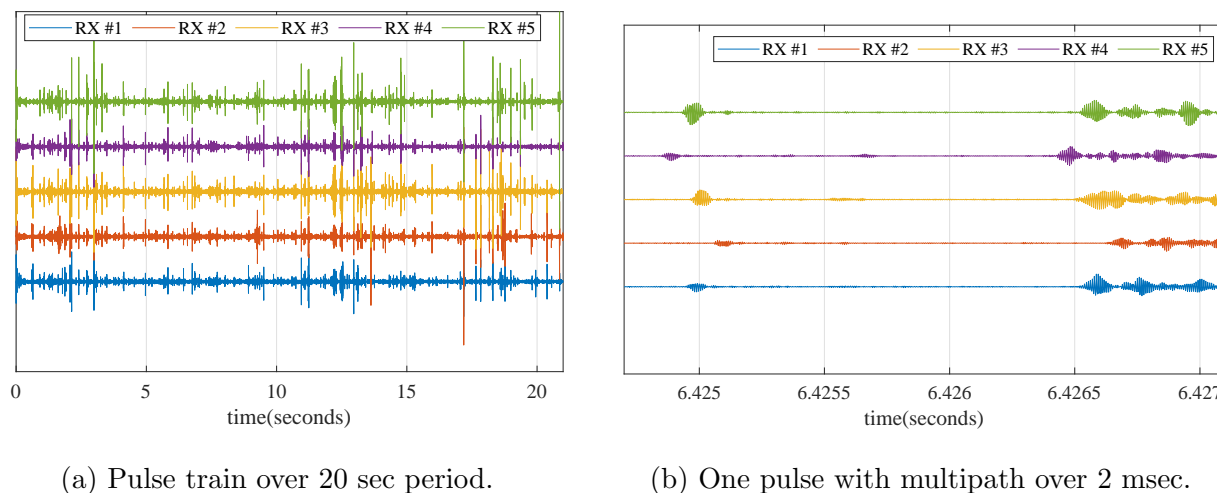


Fig. 2.6.11: Harbour porpoise echolocation sequence at 12:40pm, August 14, 2019

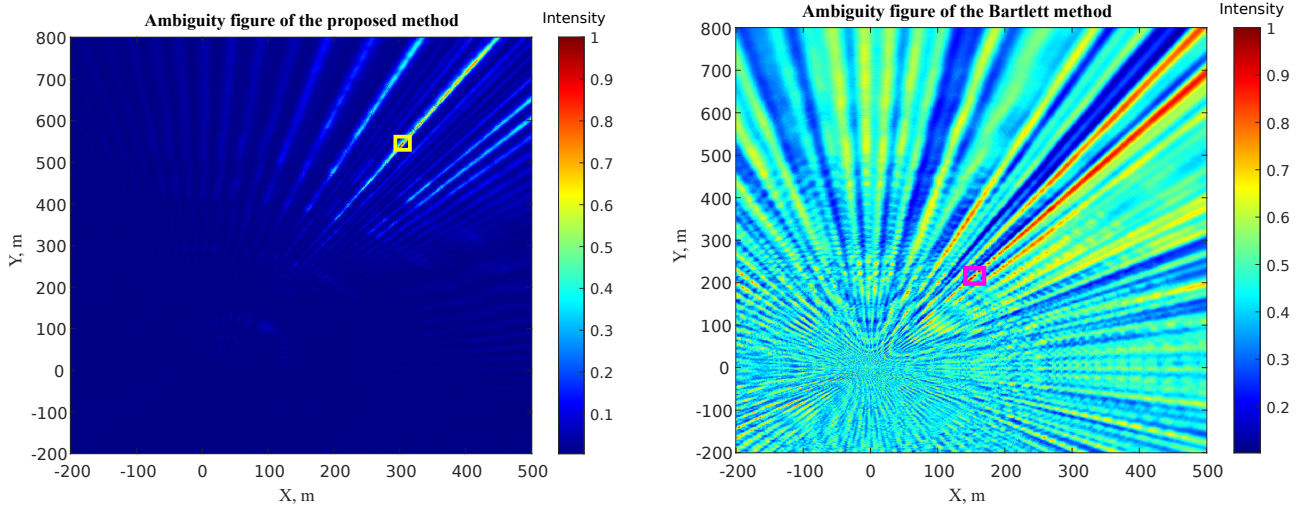
As can be seen from Fig. 2.6.11b, the received signals can be divided into two sets of arrivals. There is a delay of approximately 1.6 milliseconds between the start times of the two sets of arrivals. During this record, the research boat was moving around the hydrophone array, and the harbour porpoise was observed by the research team in close vicinity of the research vessel.

Due to the number of received pulses, the time delays and also the simulations, the Image model (6) is considered as a propagation model in the Bartlett estimator and the proposed algorithm to find the location of the harbour porpoise. The location of the harbour porpoise is found to be $\hat{p} = (306\text{m}, 548\text{m}, 0.2\text{m})$ using the proposed algorithm, and $\hat{p} = (155\text{m}, 216\text{m}, 0.1\text{m})$ using the Bartlett method. Fig. 2.6.12a and Fig. 2.6.12b show the ambiguity figures of the proposed algorithm and the Bartlett method, respectively. Note that a localization range of 580 meters is larger than quoted in literature and must be confirmed. Unfortunately, the true location of the animals could not be measured, and further simulations in presence of ambient noise will be required to validate the result. This will be part of future work.

As can be seen from Figs. 2.6.12b and 2.6.12a, the proposed algorithm has better resolution than the Bartlett method. Furthermore, the proposed algorithm has been able to reduce the effect of aliasing. It should be noted that the same frequencies in the range of 120 – 150 kHz are considered when running the Bartlett and proposed method.

The estimated location of the harbour porpoise is shown in Fig. 2.6.13. As can be observed, it is approximately in the same axis as the Transmitter Station #1, and at a greater distance.

To evaluate the accuracy of each method, the estimated locations are used to re-construct a click train at the receiver similar to that of Figure 2.6.11. For this purpose, a signal with similar characteristics as the pulse signal between 0.2 msec and 0.3 msec emitted by the harbour



(a) Proposed hybrid method at a depth of 0.2 m.

(b) Bartlett method at a depth of 0.1 m.

Fig. 2.6.12: Comparison of ambiguity functions using Bartlett and Proposed Hybrid Method

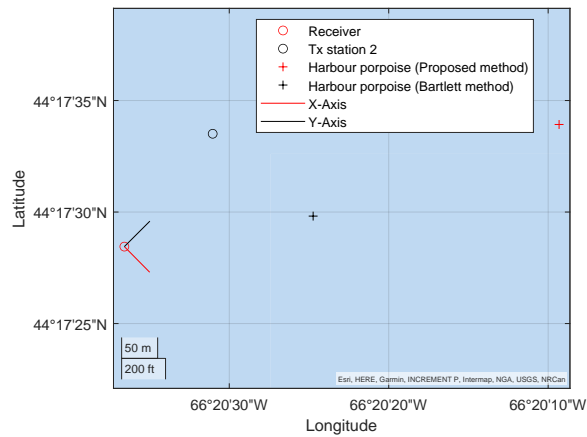


Fig. 2.6.13: Representation of the harbour porpoise location on a map.

porpoise is considered as the source point signal. Then the synthetic signals are constructed using the Image model at the locations of the hydrophones. The results are shown in Fig. 2.6.14.

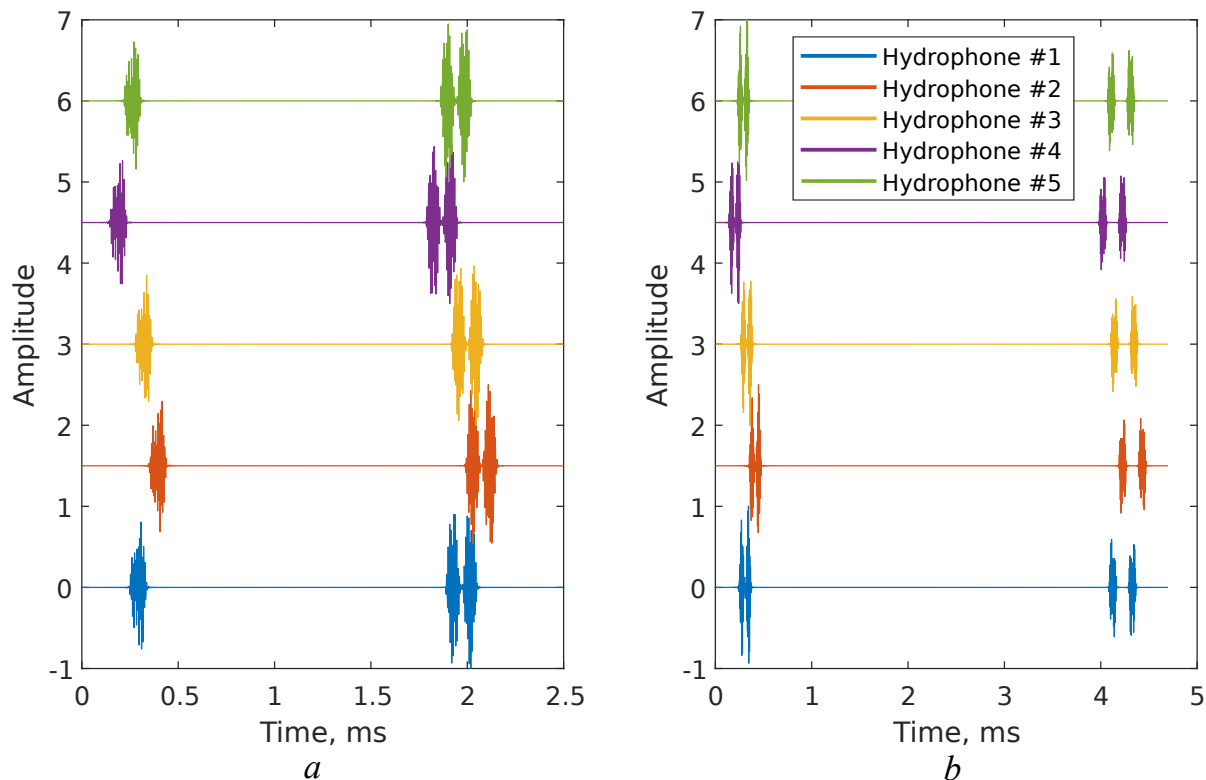


Fig. 2.6.14: Synthetic signals of the hydrophones in the time-domain.

a For the source location (306 m, 548 m, 0.2 m)

b For the source location (155 m, 216 m, 0.1 m)

As can be seen from Fig. 2.6.14, the delay between the start times of the two sets of arrivals for the source location that was found by the proposed method, like the measured signals, is approximately 1.6 milliseconds, while for the source location that was found by the Bartlett method is approximately 3.8 milliseconds. This provides an indication that the new proposed method has better accuracy than the standard frequency-domain Bartlett estimator. Further simulations that include the absorption are required to confirm that the proposed method results are valid, since previous studies indicate that the SNR would be very low at such ranges.

2.7 Real-Time System Architecture

The objective of this section is to describe the real-time system architecture for the localization algorithm. The firmware architecture including the software controller will be discussed in Section 2.7.1; then, in Section 2.7.2, the real-time localization algorithm will be detailed for implementation in VHDL; finally, in Section 2.7.3.

2.7.1 Firmware Architecture

The remote sensor is programmed on a specialized digital signal processing platform, the Zybo 7010 System-on-Chip development board. At its core, the Artix-7 Field Programmable Gate

Array (FPGA) serves to compute real-time array processing in an ultra-sonic band up to 150 kHz, with a Zynq dual-core ARM Cortex-A9 processor. This allows real-time processing of a system that can be reconfigured through software.

PetaLinux is used as the operating system for the System-on-Chip and serves as the interface between the code running on the processor, the peripherals programmed in VHDL, and a host control computer. PetaLinux is a version of the Linux kernel designed for embedded devices. It is maintained by Xilinx, and allows for easier development by providing access to the various tools and libraries included in the Linux kernel. This means it is possible to run an executable that was originally written for a Linux desktop computer on the Zybo board. The included libraries allow for easy access to files on an SD card, networking, and creating and managing multiple processes. Additionally, Linux tools for compiling code, using the network, and creating and running scripts are also available.

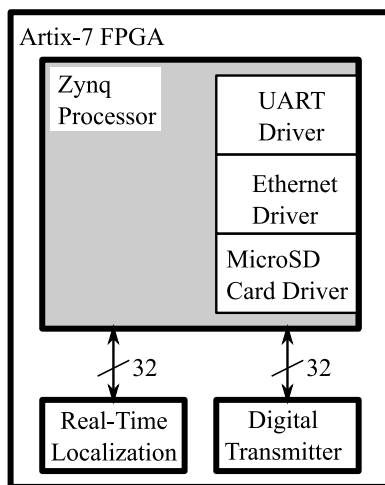


Fig. 2.7.1: Firmware architecture for the real-time remote sensor

The different peripherals that are controlled by the Zynq processor to enable the remote sensor are shown in Figure 2.7.1. The Ethernet driver is used to share high throughput information between the processor running the real-time localization algorithm with the acoustic sensor array; the Micro-SD Card driver is used to record windows containing recent harbour porpoise signatures; the Zynq processor interfaces with a peripheral programmed in VHDL that runs a marine mammal detection and localization algorithm; finally, a UART interface between the localization system and a host computer serves to send information to be displayed. An additional peripheral is available in VHDL, and includes the physical layer for a magneto-inductive communication transmitter.

For this remote sensor prototype, the real-time localization processor communicates with a 5-element acoustic recorder manufactured by Turbulent Research that can sample up to 384 ksp. Through the Ethernet interface, a network is configured to maintain a link between the Zybo FPGA board and the pressure case. This network configuration is shown in Figure 2.7.2. As can be seen, the Zybo board is connected directly to the pressure case using the Ethernet interface. The communication interface defined by Turbulent Research allows data transfer from the recorder, as well as reconfiguration of the recorder. It does this with three different protocols. The first, TracFind, is used to locate devices on the network. The second, TracIO, is used to control the device and receive important device information. The third protocol, TracStream is

used exclusively to receive the raw sound data streamed from the pressure case.

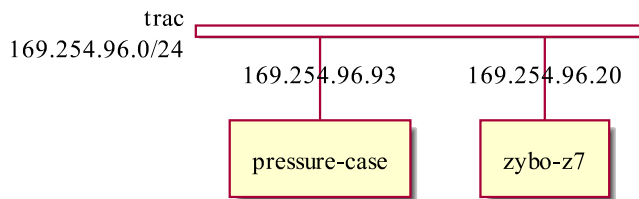


Fig. 2.7.2: Zybo network diagram

The main program running on the Zynq controls the connection to the pressure case and initiates the detection and localization algorithm. The state transition diagram for the localization program can be seen below in Figure 2.7.3. One of the main constraints for this design is the limitations imposed by the data streaming. At a sample rate of 384 kHz, it is only possible to stream on 2 channels from the pressure case. This is not enough data to determine the location of the porpoise, but it is enough to determine if a porpoise is making a sound nearby. After a porpoise sound event is detected, the data streaming stops, and the file recording begins. This file can contain many more channels (up to five), allowing for localization of the porpoise. This cycle continues forever.

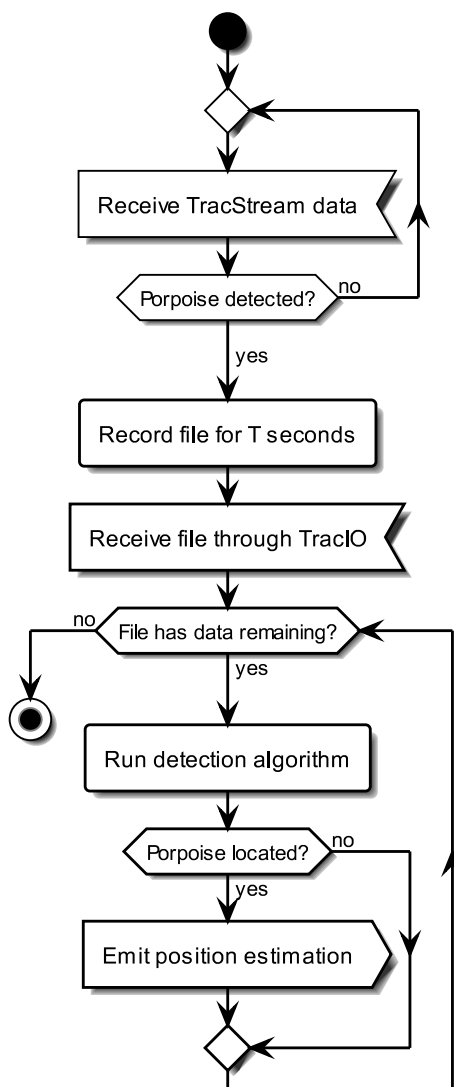


Fig. 2.7.3: Activity diagram on the Zybo board

TracFind is used to find the pressure case Trac device on the network. First, the ARM Cortex-A9 Processor sends out a UDP broadcast message requesting information on all Trac devices connected to the network. The Trac device in the pressure case responds back with critical device information including product id, revision number, MAC address, and IP address. This sequence can be seen in Figure 2.7.4.

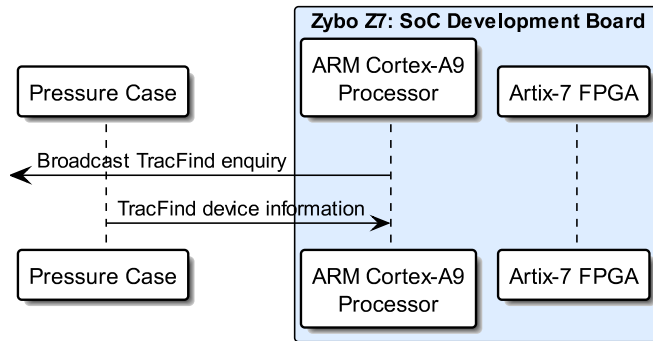


Fig. 2.7.4: TracFind program sequence diagram

Utilizing the IP address found using TracFind, the ARM processor initiates a bidirectional TCP connection to the Trac device in the pressure case. Then, the ARM processor queries the pressure case for important device information such as the protocol version, firmware version, max packet size, etc. Next, the pressure case is formatted (all existing files deleted) and set to stream on two channels. This data stream is transferred to the ARM processor which forwards it to the Artix-7 FPGA to run the detection algorithm. This data stream continues until a detection is observed and the ARM processor requests a switch from two-channel data streaming to five-channel data recording. Once this recording has been completed, the ARM processor requests for the most recent file to be transferred over. This file is stored onto the microSD card in the Zybo Development Board. Once the file transfer is complete, the ARM processor sends over short windows of channel data to the Artix-7 FPGA, which replies back with the estimated position. The ARM processor then sends this position estimation to the map display. This sequence can be seen below in Figure 2.7.5:

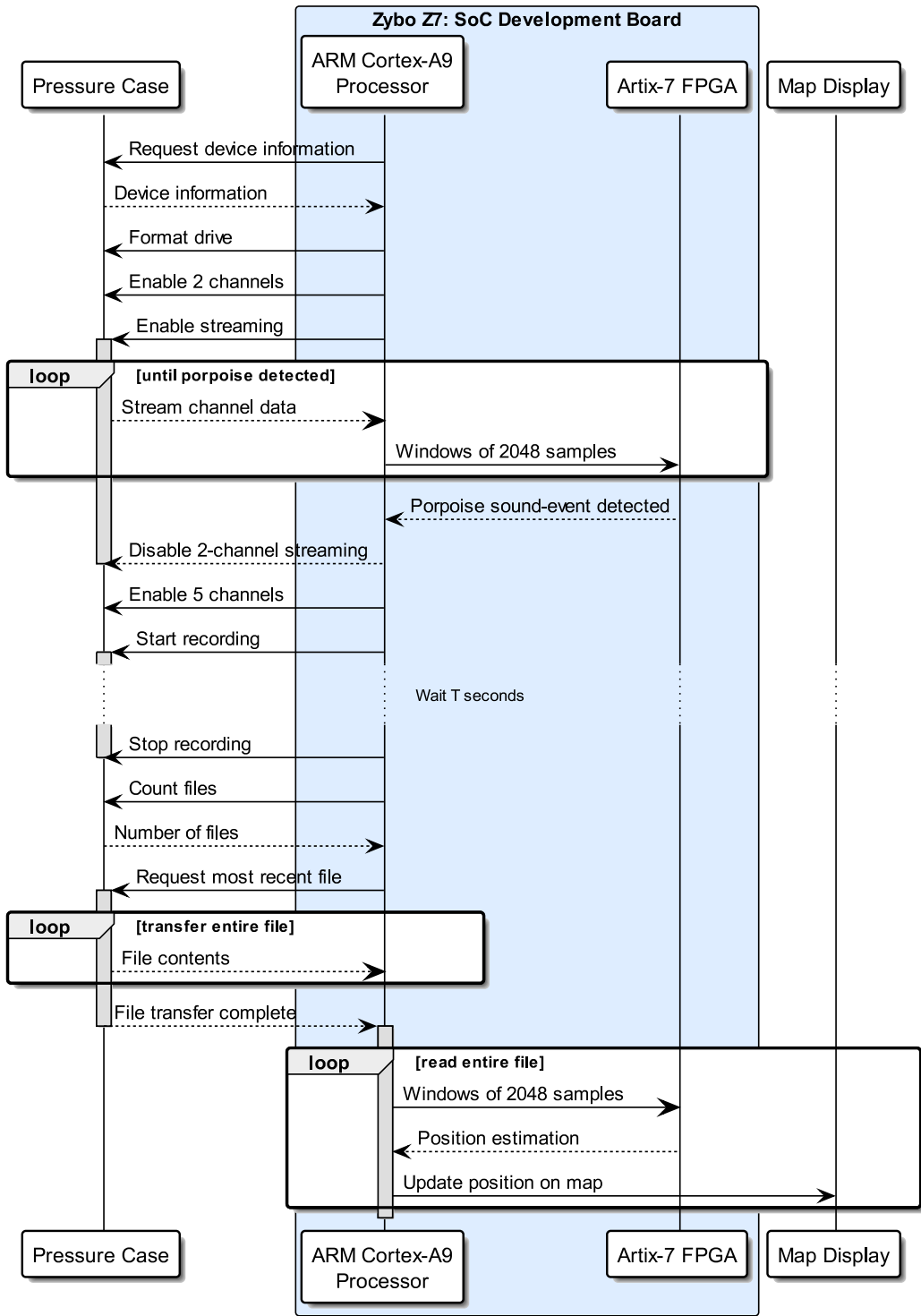


Fig. 2.7.5: Trac program sequence diagram

Note that to transfer data to a remote device, a digital transmitter is also available on the FPGA and it can be interfaced to a transceiver front-end to enable the magneto-inductive link that crosses the air-water boundary. In this work, it is interfaced with a magneto-inductive tri-axial coil, which will be described in Chapter 3. The physical layer can be configured through the software interface, which can be used to generate various signal such as a simple tone, linear

frequency modulation, M-ary phase shift keying (PSK), as well as M-ary frequency shift keying (FSK). This host computer uses a UART interface to transfer the desired signal parameters to the ARM Cortex-A9 Processor on the Zybo Z7: SoC Development Board. This processor is used to control the software-defined transmitter running on the Artix-7 FPGA. The digital output of this transmitter is applied to a pulse shaping filter to convert it to an analog signal. This analog signal is sent through a power amplifier and then ultimately to the transmitter. This architecture is shown in Figure 2.7.6.

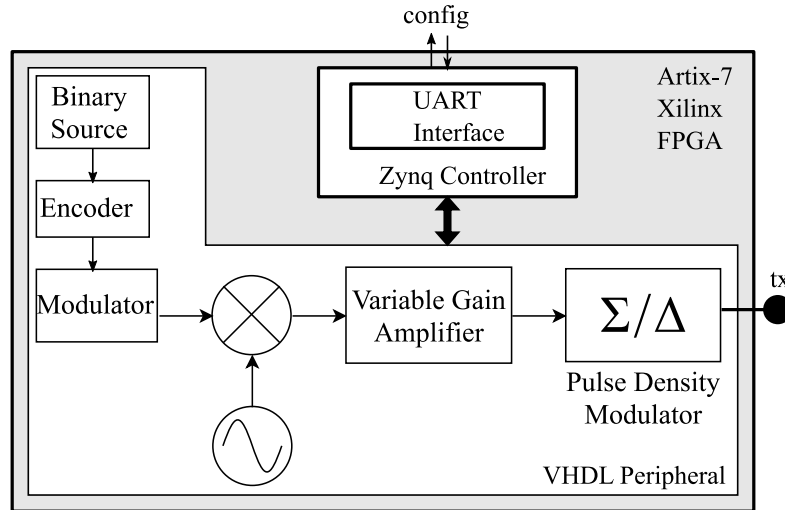


Fig. 2.7.6: Transmitter system architecture

2.7.2 Real-time Localization Implementation

Using the real-time sensor array, two goals are defined in this work:

1. Real-time detection of harbour porpoises
2. Real-time localization of harbour porpoises

The proposed localization algorithm is used for both purposes. It consists of two primary modules: the propagation model and the estimator. According to the results obtained by the proposed algorithm in MATLAB, the proposed estimator defined with Eqs. (39) to (40) in combination with the image model with at most two modes (modes 0 and 1) has been chosen to be implemented on the real-time platform.

There are some challenges in converting the proposed algorithm to a VHDL code. Resource limitation and timing issues are some of these challenges.

Resource limitations Each FPGA platform has its own capacity. This capacity includes a specific number of components. The components include Lookup Tables (LUTs), Flip-Flops (FFs), Block Ram, Digital Signal Processor slices (DSPs). Most of these components are a combination of logic gates. A VHDL code actually combines these components and connects them to each other. The FPGA board that is considered for the present work is the Zybo Z7-20. It contains 53200 LUTs, 106400 FFs, a 630-kB block RAM, and 220 DSPs.

Timing issues A VHDL program utilizes the components available (or more precisely a combination of logic gates) by providing routing between them. The transmission from the start point of the interconnected components to the endpoint has a delay. The amount of delay depends on the number of gates, the architecture of the interconnection, the length of the paths, and the technology of the gates. For example, a standard multiplication between two 16 fixed point numbers can take on the order of one nanosecond.

Typically, the signals at the output of different operations are registered so that can be used later in other combinations. To register a signal, a clock is needed. A clock is a square wave with a high value of 1 and a low value of 0 and with a specific frequency. The clock frequency in an FPGA board is adjustable.

It is important that a signal is stable before the clock changes from 0 to 1 or 1 to 0. Therefore, a timing issue appears if the clock cycle is very short so that the signals cannot be registered. There are some ways to solve this issue, which will be explained later.

To have the maximum running speed, the algorithm should be optimized in both arithmetic and programming. The simpler the mathematics implies utilizing less amount of resources. Next, a simplification for the proposed localization estimator is proposed.

Review of the proposed localization estimator algorithm

Equation (39) can be simplified as

$$\mathbf{C}_c(p) \approx \frac{1}{2} \sum_{l_f} \left(\left[\left[\text{Re} \{ \bar{\mathbf{T}}_1(l_f, p) \} \right]^\top \left[\text{Re} \{ \bar{\mathbf{T}}_1(l_f, p) \} \right] \right] + \left[\left[\text{Im} \{ \bar{\mathbf{T}}_1(l_f, p) \} \right]^\top \left[\text{Im} \{ \bar{\mathbf{T}}_1(l_f, p) \} \right] \right] \right), \quad (41)$$

where $\bar{\mathbf{T}}_1(l, p) = \frac{\Delta\omega}{2\pi} \epsilon_l \bar{\mathbf{S}}(\omega_l, p)$.

This simplification is obtained because the following equations hold.

$$\sum_{k=0}^{L-1} (\text{Re} \{ \bar{T}_2(l_f, k) \})^2 = \sum_{k=0}^{L-1} (\text{Im} \{ \bar{T}_2(l_f, k) \})^2 = \frac{L}{2}, \quad (42)$$

$$\sum_{k=0}^{L-1} (\text{Re} \{ \bar{T}_2(l_f, k) \} \text{Im} \{ \bar{T}_2(l_f, k) \}) = 0, \quad (43)$$

where $\bar{T}_2(l, k) = e^{-i(\frac{2\pi lk}{L} + \omega_l t_{\min})}$. It should be noted that, if $\mathbf{T}_1(l, k)$ and $T_2(l, k)$ are respectively replaced by $\bar{\mathbf{T}}_1(l, k)$ and $\bar{T}_2(l, k)$ in (39) then the result does not change.

Proof of (42):

$$\begin{aligned} \sum_{k=0}^{L-1} (\text{Re} \{ \bar{T}_2(l_f, k) \})^2 &= \sum_{k=0}^{L-1} \left(\cos \left(\frac{2\pi lk}{L} + \omega_l t_{\min} \right) \right)^2 = \sum_{k=0}^{L-1} \left(\frac{1 + \cos \left(\frac{4\pi lk}{L} + 2\omega_l t_{\min} \right)}{2} \right) \\ &= \frac{L}{2} + \frac{1}{2} \sum_{k=0}^{L-1} \cos \left(\frac{4\pi lk}{L} + 2\omega_l t_{\min} \right) = \frac{L}{2} \end{aligned}$$

Since the period of $\cos(\frac{4\pi lk}{L} + 2\omega_l t_{\min})$ is $\frac{L}{2l}$, $\sum_{k=0}^{L-1} \cos(\frac{4\pi lk}{L} + 2\omega_l t_{\min})$ is a summation over $2l$ periods. Therefore if $l \neq \frac{\bar{a}L}{2}$ then $\sum_{k=0}^{L-1} \cos(\frac{4\pi lk}{L} + 2\omega_l t_{\min}) = 0$, where \bar{a} is any arbitrary integer number. As we know, l which is the index of frequency, takes the values $0, 1, \dots, \frac{L}{2} - 1$, then (42) is always true for all the frequencies we use.

If $l = \frac{\bar{a}L}{2}$ then $\cos(\frac{4\pi lk}{L} + 2\omega_l t_{\min}) = \cos(2\pi k\bar{a} + 2\omega_l t_{\min}) = \cos(2\omega_l t_{\min})$ is a constant value (i.e. it is not a periodic function). Therefore, the summation of $\cos(2\omega_l t_{\min})$ over $[0, L - 1]$ is not always zero.

Similarly

$$\begin{aligned} \sum_{k=0}^{L-1} (\text{Im} \{ \bar{T}_2(l_f, k) \})^2 &= \sum_{k=0}^{L-1} \left(\sin\left(\frac{2\pi lk}{L} + \omega_l t_{\min}\right) \right)^2 = \sum_{k=0}^{L-1} \left(\frac{1 - \cos\left(\frac{4\pi lk}{L} + 2\omega_l t_{\min}\right)}{2} \right) \\ &= \frac{L}{2} - \frac{1}{2} \sum_{k=0}^{L-1} \cos\left(\frac{4\pi lk}{L} + 2\omega_l t_{\min}\right) = \frac{L}{2} \end{aligned}$$

Proof of (43):

$$\begin{aligned} \sum_{k=0}^{L-1} (\text{Re} \{ \bar{T}_2(l_f, k) \} \text{Im} \{ \bar{T}_2(l_f, k) \}) &= - \sum_{k=0}^{L-1} \left(\cos\left(\frac{2\pi lk}{L} + \omega_l t_{\min}\right) \sin\left(\frac{2\pi lk}{L} + \omega_l t_{\min}\right) \right) = \\ &= - \frac{1}{2} \sum_{k=0}^{L-1} \left(\sin\left(\frac{4\pi lk}{L} + 2\omega_l t_{\min}\right) \right) = 0 \end{aligned}$$

These simplifications provide more efficient and higher speed localization in the implementation on the FPGA.

In addition to reducing the algorithm complexity, a number of solutions are being adopted to address limited resources on the FPGA. A first exercise consists in optimizing number representation on the FPGA; fixed-point representation with a limited number of bits is generally preferable, and only in very specific cases is a floating point number utilized, particularly when the data spans a wide range. This requires the analysis of the different parts of the equations. Secondly, it is possible to re-use operators for different inputs, particularly those operators that have more complex implementation, such as the CORDIC, and the FFT. Thirdly, clocked processes can be used to pipeline operations, at the cost of latency.

Our design is also constrained on time. In the proposed localization algorithm, several loops are required to estimate the location of an acoustic source. The loops are used to sweep several vectors including azimuth, range, depth, sensor index, path (of the image model), and frequency.

The received time signals at the hydrophones are converted to the frequency domain spectrum using an FFT core in the FPGA board. Note that the FFT size and the sampling frequency are 2048 and 384 kHz, respectively. Therefore, the bin size of the spectrum is calculated to be 187.5 Hz. The clicks generated by a harbour porpoise are in the frequency range of about 120 to 150 kHz. Hence, there are about 160 frequency bins in this range.

The search area for the localization is a cylinder around the hydrophone array with a radius of 1000 m, and its height is equal to the sea depth. Therefore, the azimuth is swept between

-180 and 180 degrees in steps of at least 1 degree, the range is swept between 1 m to 1000 m in steps of about 1 m, and the depth is swept between 0 to 20 m if the sea depth is 20 m in steps of about 0.1 m.

Four sensors are considered to obtain an accurate estimation of the localization. A simple calculation shows that 368640×10^6 (360 Azimuth points \times 1000 Range points \times 200 Depth points \times 160 Frequency points \times 4 Sensors \times 8 Paths) loops are required to have a complete estimation. If we assume that each loop takes about 5 ns (the clock frequency of 200 MHz), then an estimation takes about 30 minutes which is a very long time. This is assuming there are no additional delays between the start and the endpoints. In reality, there are additional logic and wire delays, and so the situation becomes worse in terms of time.

Several ways are considered in the present work to maintain real-time estimation.

First, although using a combinatorial logic requires many resources rather than clocked processes, we use the combinatorial logic in this project. Because, firstly there are enough amount of resources in the Z7-20 board to do the main operations, secondly because a combinatorial logic is not registering data before and after each component (except the start point of the first component and the endpoint of the last component), it is much faster than a clocked process.

Second, instead of having the calculations of the hydrophones in loops, they are performed in parallel. This means using four parallel combinatorial logic components which require many resources. In this way, the number of sensors, that is 4, is eliminated from the loop calculation.

Third, instead of having all the calculations in a single block design, which is equivalent to having all the calculations in each loop, multiple block designs are considered. In this way, the calculations that do not have some specific variable are not necessarily needed to be performed in the loops of those parameters. For example, the conversion from the (Azimuth, Range) pair to the (X, Y) pair, that is $X = range \times \cos(azimuth)$, $Y = range \times \sin(azimuth)$ does not depend on the frequency, and therefore it is not needed to be performed in the loops of frequency. Figure 2.7.7 shows an overview of the explained methodology.

Fourth, instead of using all the frequency bins (160 frequency bins in the present work), we can define a threshold in terms of the magnitude values of the spectrum to eliminate the smallest ones from the calculation. This idea has not been tested yet.

Fifth, scenarios are considered to reduce the number of search point. In each scenario the localization algorithm is performed for a small portion of the search space. Then, in the next scenario the search space is a limited area around the location that was estimated from the previous scenario. The scenarios are defined as follows.

1. Scenario #1: Range is considered as a long-range, for example, greater than 2000 m, Depth is considered as 0.2 m, and Azimuth is swept from 1 to 360 degrees each 1 degree. This implies 360 search points.
2. Scenario #2: Azimuth is swept from -10 to 10 degrees around the estimated Azimuth. Depth takes the values 1, 4, 7, 10, 13, 16, 19 m in each loop. Range takes the values 100, 150, 200, 250, ..., 1000 m in each loop. This implies 2660 search points.
3. Scenario #3: Azimuth is considered as the estimated Azimuth. Depth is swept ± 5 m around the estimated Depth each 0.5m. Range is swept ± 100 m around the estimated Range each 1m. This implies 4221 search points.
4. Scenario #4: Azimuth is swept ± 0.25 degrees around the estimated Azimuth each 0.25

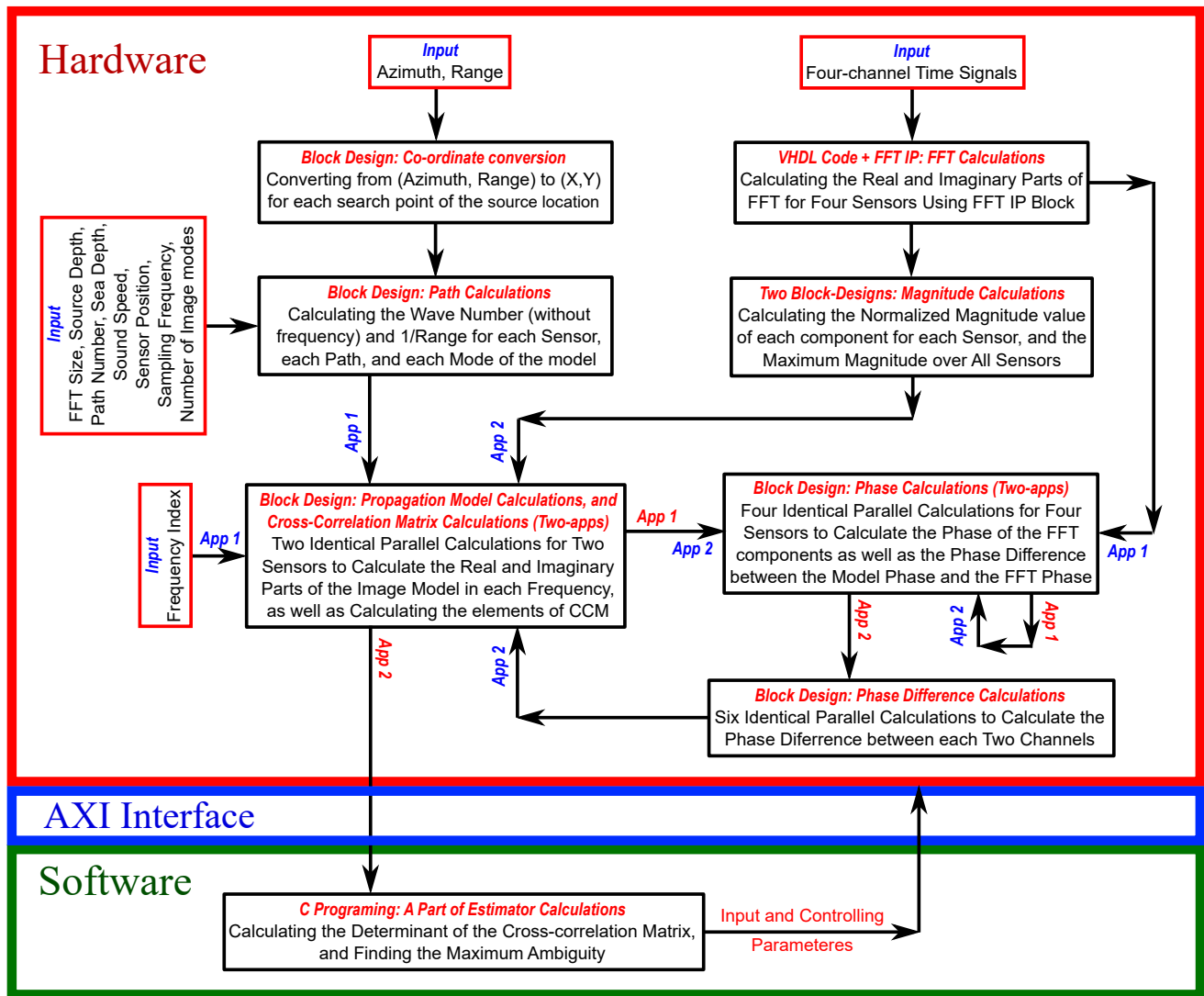


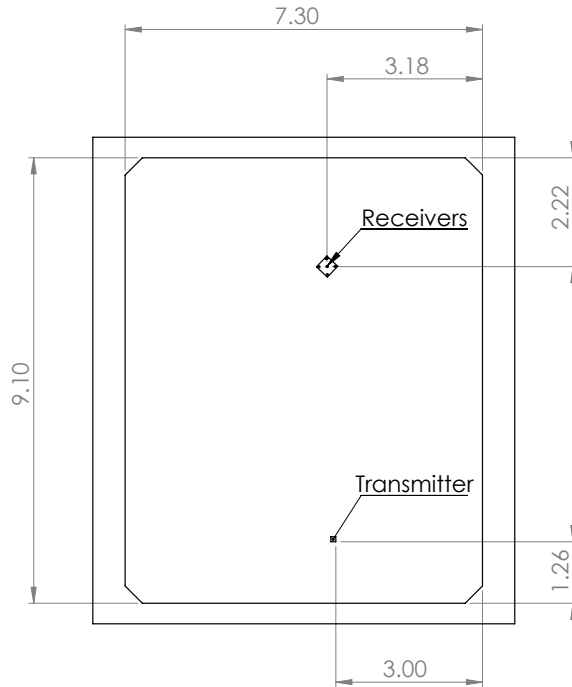
Fig. 2.7.7: An overview of the block separation

degrees. Depth is swept ± 1.5 m around the estimated Depth each 0.1m. Range is swept ± 20 m around the estimated Range each 1m. This implies 3813 search points.

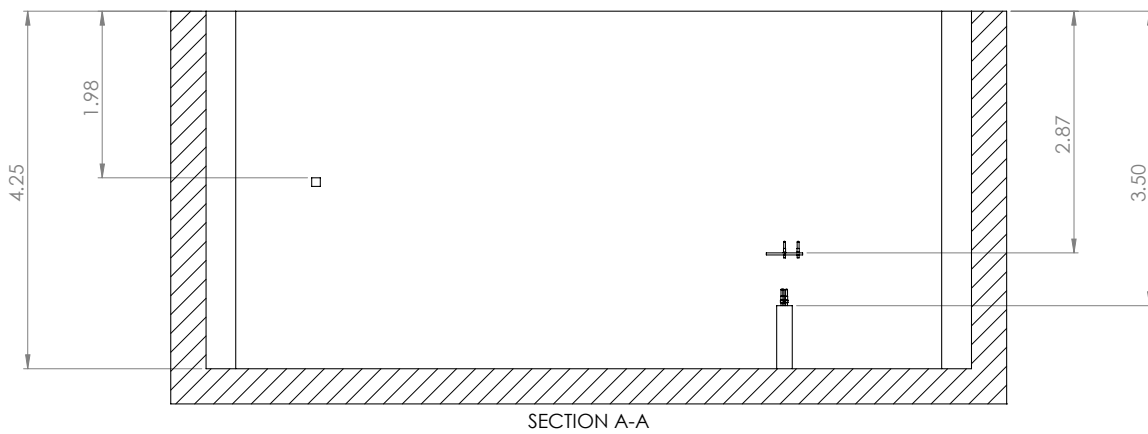
Therefore the number of loops for the search space is reduced by a factor of 6500 from 72×10^6 search points to 11054 search points.

2.7.3 Verification of the Controller in Test Tanks

To verify the proper operation of the localization system, it was deployed in a controlled environment. These tests were performed in a rectangular tank at the Aquatron in Dalhousie University. The tank, filled with sea water, measured 7.3 m by 9.1 m with a maximum depth of 4.25 m. During the tests, the water surface was 0.50 m below the top of the tank, leading to an effective depth of 3.75 m. The single transmitter was positioned near the middle of one of the 7.3 m edges of the tank at a depth of 1.47 m, while the five-receiver array was positioned near the middle of the opposite edge anchored to the bottom of the tank. A top view of the deployment is shown in Figure 2.7.8a and a side view is shown in Figure 2.7.8b.



(a) Top View



(b) Side View

Fig. 2.7.8: Illustration of the Aquatron Deployment Geometry

The five-receiver array was composed of two horizontal planes of receivers. The bottom plane had three receivers in a “T” formation, where each receiver was 4.4 cm away from the centre of the array. The top plane was 24.7 cm above the bottom plane and had two receivers, one in the centre of the array and one 16.1 cm away towards the closest wall of the tank. This geometry was chosen as it closely resembles the proposed geometry to be deployed and should allow for estimation of range, bearing, and depth. This geometry can be seen in Figure 2.7.9.

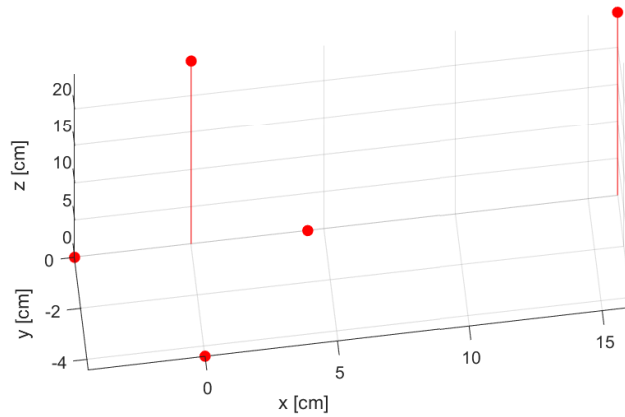


Fig. 2.7.9: Aquatron hydrophone geometry

The first tests performed were performed in air. This test involved turning on the controller in the pressure case and connecting the case directly to a host laptop. The laptop was used to issue several commands to ensure proper functionality of all subsystems including data streaming, file recording, file saving, and file transferring. All of these tests were performed using the Trac software provided by Turbulent Research.

After the initial set of air tests were executed successfully, the Trac software was used to start a file recording. Once recording commenced, the pressure case was submerged into the pool and maneuvered into the position previously indicated in Figure 2.7.8a. The recording lasted the entire duration of the transmission and localization tests, only stopping after the pressure case was brought back to the surface. This recording captured on 5 channels and included recordings of the transmission and localization tests.

The localization test was performed by repeatedly sending a 20 ms snippet of a 27.5 kHz sine wave every 1 second. This signal is a low-frequency approximation of the clicks emitted by harbour porpoises, which each last 50-600 microseconds and are centred around 130-140 kHz. The arrivals of these bursts measured at each hydrophone allow us to determine the position of the sound source. This train of bursts for one element of the array can be seen in Figure 2.7.10.

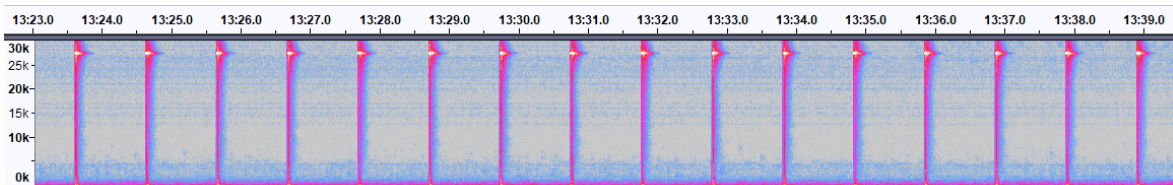


Fig. 2.7.10: 27.5 kHz burst arrivals

This test revealed that connecting the FPGA directly to the power amplifier for the transmitter leads to a very poor transient response at the start of each burst. This transient response was improved upon by inserting an op-amp to both buffer the signal output by the FPGA and amplify it by a factor of 2. This leads to a much cleaner transient response, since the power amplifier is not directly loading the output of the FPGA.

The protocol tests were run by first querying the device for important device information including the IP address, firmware version, available features using TracFind and TracIO. The result of the TracFind test shows that the TR Acoustic Device is accessible at an IP address of 169.254.96.94. This IP address was used to successfully create a TracIO connection with the TR Acoustic Device. Using this connection, the device announced it was capable of all required features such as acquiring data on 5 channels, recording, and streaming. However, it does not support optional features such as the dual sample rate mode, advanced file manipulation, and the sampling high pass filter.

Then, the second test was run to enable data streaming on two channels sampled at 96 kHz with a gain of 30.0 dB. This data stream was saved for a duration of 100 ms and stored in a file on a host computer containing the raw channel data for both channels. The protocol was then used to disable this data stream. This test was repeated for a total of three occurrences, successfully demonstrating that the protocol can be used to acquire raw channel data in real time.

During the next test, a file was recorded containing four channels sampled at 96 kHz each with a gain of 30.0 dB. This data was recorded and saved directly to the SSD in the pressure case. After recording for 30 seconds, the protocol was used to disable the file recording. The protocol was then used to transfer over the 30 seconds of data recorded using four hydrophones to a host computer. Additionally, this recorded data was also transferred using the Trac software provided by Turbulent Research. The files obtained using the protocol and the Trac software were then compared and found to be identical. This test demonstrated that the protocol can be used to record and obtain raw channel on four channels.

Finally, all of these tests were integrated together and performed sequentially. First, data streaming on two channels was sampled at a frequency of 96 kHz. Similar to the second test, this data was saved for 100 ms on a host computer. Then, the data from four hydrophones was recorded onto the internal SSD for a duration of 30 seconds. This file was then transferred over to a host computer using the protocol. This test was repeated for a total of five occurrences. This test demonstrated that the software can successfully utilize both modes of operation (streaming and recording) and can switch between them at any time.

Overall, these tests demonstrated that the Trac protocol can be used in an underwater environment similar to that of the planned final deployment. This started by successfully finding and creating a connection to the TR Acoustic Device. Using this connection, the two mode of operation were successfully demonstrated both individually and integrated together. These two modes of operation will allow for porpoise detection using the data from two hydrophones and porpoise localization using the data from four hydrophones.

3 Magneto-Inductive Coupling

To forward the events in real-time, in this work a wireless communication link is proposed and a permanent link should be established, so that the sensor array at the bottom of the ocean can forward the information to an end user. Because the Bay of Fundy is subject to high flow, modems that are attached to a surface buoy are subject to harsh conditions, and the motion can cause damage to the devices. Instead, in this work, an aerial drone is proposed to capture localization messages from the sensor devices underwater. The payload to be transmitted includes the range, bearing and depth estimate, and upon detection, this information can be sent for example on a 5-second period. Assuming the payload is represented on 8 bytes, the average data throughput that the link must sustain is 12.8 bps. The challenge here is to develop a wireless link from the bottom mounted sensor, travel approximately 20 meters underwater, and cross the air-water interface. The aerial drone is expected to be at most 10 meters above the surface. For this purpose, magneto-inductive coupling is proposed and a transmitter with a 1-W power budget is considered.

In this section, a preliminary design of the communication link will be developed. For this purpose, in Section 3.1, a geometry for the MI transducers to reach the aerial drone will be evaluated using realistic models of the communication link underwater. In this preliminary analysis, the link capacity is the figure of merit utilized. Further, in Section 3.4, a plan to validate the link range will be run, and the current status of the MI test setup will be described.

3.1 Analytical Model

3.1.1 Initial Setup

Refer to figure 3.1. Cylindrical coordinates (s, ϕ, z) are used with the origin on the boundary. The transmitter (TX) coil is placed underwater at a depth d below the surface. The centre is located at the point $(0, 0, -d)$ and is parallel to the boundary. The receiver (RX) coil is placed at a height h above the surface. The centre is located at the point $(0, 0, h)$ and is also parallel to the air-water boundary. Both coils have radius α and have N turns, but the thickness are small enough that they can be modelled with no thickness. However, no assumption is made where α is small enough to approximate the coils as magnetic dipoles.

The permittivity of the air is assumed to be the same as in vacuum and has no electrical conductivity. The water has a complex permittivity $\epsilon_w = \epsilon_{rw}\epsilon_0 + \sigma/2\pi f$ where the dielectric constant is $\epsilon_{rw} = 81$ and the conductivity of water is $\sigma = 4 \text{ S/m}$.

The TX coil is powered with an AC current of the form $I(t) = \text{Re}(Ie^{j2\pi ft})$. Here, I is a fixed amplitude. The goal is to find the induced voltage $V(t) = \text{Re}(V(f)e^{j2\pi ft})$ in the RX coil.

3.1.2 Deep Water Solution

The first step is to find the frequency dependant magnetic field \mathbf{H} created by the TX coil. Initially assume that the TX coil is in deep water. Solve the inhomogeneous Maxwell's equations in linear

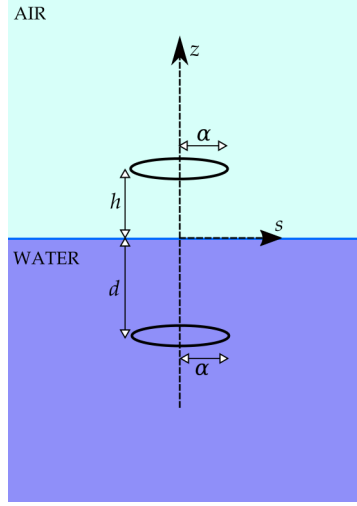


Fig. 3.1: Diagram of the the transmission coils.

media in the frequency domain:

$$\nabla \cdot \mathbf{E} = \rho \quad (44a)$$

$$\nabla \times \mathbf{E} = -j2\pi f\mu_0\mathbf{H} \quad (44b)$$

$$\nabla \cdot \mathbf{H} = 0 \quad (44c)$$

$$\nabla \times \mathbf{H} = \mathbf{J} + j2\pi f\epsilon_w\mathbf{E} \quad (44d)$$

There are no free charges, so $\rho = 0$. The current density comes from the TX coil and can be modelled as:

$$\mathbf{J} = NI\delta(s - \alpha)\delta(z + d)\hat{\phi} \quad (45)$$

Maxwell's equation can be simplified by introducing the vector potential, \mathbf{A} :

$$\mathbf{H} = \frac{1}{\mu_0}\nabla \times \mathbf{A}, \quad \nabla \cdot \mathbf{A} = 0 \quad (46)$$

Substitute (45) and (46) into (44) to get:

$$\nabla^2 \mathbf{A} + k_w^2 \mathbf{A} = -\mu_0\mathbf{J} \quad (47)$$

where $k_w^2 = (2\pi f)^2\epsilon_w\mu_0$ is the complex wavenumber in water.

To solve (47), the symmetry of the problem must be taken advantage. Since the z -axis goes through the centre of the TX coil and is orthogonal to the plain of the coil, any rotation around the z -axis does not change \mathbf{J} . Thus \mathbf{A} must be independant of ϕ . Also \mathbf{J} only has a $\hat{\phi}$ -component and therefore so does \mathbf{A} . The vector potential can be written as $\mathbf{A} = A\hat{\phi}$. The resulting simplification gives:

$$\frac{\partial^2 A}{\partial s^2} + \frac{1}{s}\frac{\partial A}{\partial s} - \frac{1}{s^2}A + \frac{\partial^2 A}{\partial z^2} + k_w^2 A = -\mu_0 NI\delta(s - \alpha)\delta(z + d) \quad (48)$$

This equation can be solved by taking a Fourier transform in z , followed by an order-1 Hankel transform in s . The result is:

$$A = \frac{j\mu_0 NI\alpha}{2} \int_0^\infty \frac{k}{K_w} J_1(k\alpha) J_1(ks) e^{jK_w|z+d|} dk \quad (49)$$

where $K_w = \sqrt{k_w^2 - k^2}$. Observe that the solution is a weighted superposition of cylindrical waves of complex wavevector $\mathbf{k} = k\hat{s} + K_w\hat{z}$. The s -component of \mathbf{k} is used as the variable of integration.

Substituting (49) back into (46) to get the magnetic field of a coil in deep water:

$$\mathbf{H} = H_s\hat{s} + H_z\hat{z} \quad (50a)$$

$$H_s = \frac{NI\alpha}{2} \int_0^\infty k J_1(k\alpha) J_1(ks) e^{jK_w|z+d|} dk \quad (50b)$$

$$H_z = \frac{jNI\alpha}{2} \int_0^\infty \frac{k^2}{K_w} J_1(k\alpha) J_0(ks) e^{jK_w|z+d|} dk \quad (50c)$$

$$K_w = \sqrt{k_w^2 - k^2} \quad (50d)$$

Again, note that this solution is a weighted superposition of cylindrical waves of complex wavevector $\mathbf{k} = k\hat{s} + K_w\hat{z}$.

The electric field can be found by $\mathbf{E} = -j2\pi f\mathbf{A}$. Thus $\mathbf{E} = E\hat{\phi}$, where:

$$E = \pi\mu_0 NI\alpha f \int_0^\infty \frac{k}{K_w} J_1(k\alpha) J_1(ks) e^{jK_w|z+d|} dk \quad (51)$$

Assuming $z > -d$, (50) and (51) can be rewritten as:

$$\mathbf{E} = \int_0^\infty E_i(k) J_1(ks) e^{jK_w z} \hat{\phi} dk \quad (52a)$$

$$\mathbf{H} = \int_0^\infty \frac{E_i(k)}{2\pi\mu_0 f} [K_w J_1(ks) e^{jK_w z} \hat{s} + jk J_0(ks) e^{jK_w z} \hat{z}] dk \quad (52b)$$

where $E_i(k) = \pi\mu_0 NI\alpha f \frac{k}{K_w} J_1(k\alpha) \exp(jK_w d)$. These equations show explicitly the wave structure. This will be important in the next section.

3.1.3 Crossing the Air-Water Interface

Maxwell's equations are linear in \mathbf{E} and \mathbf{H} . Therefore the general solution to (44) in a given medium can be written as a linear combination of a homogeneous solution and a particular solution:

$$\mathbf{E} = \mathbf{E}_{homo} + \mathbf{E}_{part} \quad (53a)$$

$$\mathbf{H} = \mathbf{H}_{homo} + \mathbf{H}_{part} \quad (53b)$$

In deep water, \mathbf{E}_{part} , and \mathbf{H}_{part} are given by (51) and (50). The homogeneous solutions in this case are zero. Once a second medium (air) and a boundary are introduced, the homogeneous solutions can no longer equal zero in order for the boundary conditions to be met.

Let m be an index to indicate which medium. $m = 0$ for air and $m = w$ for water. The general structure of the homogeneous solution in a given medium with permittivity ϵ_m is found by solving (44) with $p = 0$ and $\mathbf{J} = 0$, which is equivalent to finding a family of solutions to the wave equations:

$$\nabla^2 \mathbf{E}_{homo} + k_m^2 \mathbf{E}_{homo} = 0 \quad (54a)$$

$$\nabla^2 \mathbf{H}_{homo} + k_m^2 \mathbf{H}_{homo} = 0 \quad (54b)$$

$$k_m^2 = (2\pi f)^2 \epsilon_m \mu_0 \quad (54c)$$

Equation (52) implies that cylindrical transverse-electric waves (i.e. cylindrical waves where \mathbf{E} are parallel to the boundary) are the only non-zero solutions to the wave equations.

$$\mathbf{E}_{homom} = \int_0^\infty E_m(k) J_1(ks) e^{jK_m z} \hat{\phi} dk \quad (55a)$$

$$\mathbf{H}_{homom} = \int_0^\infty \frac{E_m(k)}{2\pi\mu_0 f} [K_w J_1(ks) e^{jK_w z} \hat{s} + jk J_0(ks) e^{jK_w z} \hat{z}] dk \quad (55b)$$

The coefficients $E_m(k)$ for $m = 0$ and $m = w$ must be found via the boundary conditions.

The \mathbf{H} -field from the TX coil underwater is only needed. Thus it is assumed that there are no sources in the air. Therefore, for $z > 0$, \mathbf{E} and \mathbf{H} are only given by the homogeneous solution (55) with $m = 0$. In the water (i.e. $z < 0$), \mathbf{E} and \mathbf{H} are given by combining (55) with $m = w$ and (52):

$$\mathbf{E} = \int_0^\infty [E_i(k) + E_w(k)] J_1(ks) e^{jK_m z} \hat{\phi} dk \quad (56a)$$

$$\mathbf{H} = \int_0^\infty \frac{E_i(k) - E_w(k)}{2\pi\mu_0 f} [K_w J_1(ks) e^{jK_w z} \hat{s} + jk J_0(ks) e^{jK_w z} \hat{z}] dk \quad (56b)$$

The boundary conditions can be found from the integral form of Maxwell's equations. They are summarized here for a boundary at $z = 0$:

$$\mathbf{E}_\perp^{water} \epsilon_w = \mathbf{E}_\perp^{air} \epsilon_0 \quad (57a)$$

$$\mathbf{E}_\parallel^{water} = \mathbf{E}_\parallel^{air} \quad (57b)$$

$$\mathbf{H}^{water} = \mathbf{H}^{air} \quad (57c)$$

Apply this to get the following relations:

$$E_w(k) = E_i(k) \frac{K_w(k) - K_0(k)}{K_w(k) + K_0(k)} \quad (58)$$

$$E_0(k) = E_i(k) \frac{2K_w(k)}{K_w(k) + K_0(k)} \quad (59)$$

Substitute these equations back into (56) and (55) to get the complete solution for the \mathbf{H} -field in air ($z > 0$):

$$\mathbf{H} = NI\alpha \int_0^\infty \frac{k}{K_w + K_0} J_1(k\alpha) e^{jK_w d} [K_0 J_1(ks) e^{jK_0 z} \hat{s} + jk J_0(ks) e^{jK_0 z} \hat{z}] dk \quad (60)$$

where $K_w = \sqrt{(2\pi f)^2 \epsilon_w \mu_0 - k^2}$ and $K_0 = \sqrt{(2\pi f)^2 \epsilon_0 \mu_0 - k^2}$.

3.1.4 Magnetic Induction

The mutual inductance of the receiver coil is given by:

$$M(f) = \mu_0 \Phi_{coil} / I_{TX} \quad (61)$$

where Φ_{coil} is the magnetic flux across the coil and is given by:

$$\Phi_{coil} = \iint_{\text{coil cross-section}} \mathbf{H} \cdot d\mathbf{a} \quad (62)$$

The cross section of the RX coil consists of N superimposed disks of radius α perpendicular to the z -axis (so $d\mathbf{a} = s ds d\phi \hat{z}$) located at $z = h$. Thus (62) simplifies to:

$$\Phi_{coil} = N \int_{\phi=0}^{2\pi} \int_{s=0}^{\alpha} H_z(s, z = h) s ds d\phi \quad (63)$$

Substitute (60) into this equation to get the final answer:

$$M_{Forget} = j2\pi\mu_0 N_{TX} N_{RX} \alpha_{RX} \int_0^{\infty} \frac{x J_1(x) J_1\left(\frac{\alpha_{RX}}{\alpha_{TX}} x\right) e^{\left[\frac{d}{\alpha_{TX}} \sqrt{(\epsilon\Omega + j\Sigma)\Omega - x^2} + \frac{h}{\alpha_{TX}} \sqrt{\Omega^2 - x^2}\right]}}{\sqrt{(\epsilon\Omega + j\Sigma)\Omega - x^2} + \sqrt{\Omega^2 - x^2}} dx \quad (64)$$

where the following parameters are defined:

$x = k\alpha_{TX}$	New dimensionless variable of integration.
$\epsilon_{rw} = \text{Re}[\epsilon_w]/\epsilon_0$	Dielectric constant of water.
$\Omega = 2\pi\alpha_{TX}f/c$	Dimensionless frequency parameter.
$\Sigma = \mu_0 c \alpha_{TX} \sigma$	Dimensionless conductivity parameter.

3.1.5 Comparison with Gibson's Model

Gibson [11] presented a model from Wait for the mutual induction with the assumption that the coils are far away $\alpha_{TX}, \alpha_{RX} \ll d + h$ from each other.

$$M_{Gibson} = \frac{\pi\mu_0 N_{TX} N_{RX} \alpha_{TX}^2 \alpha_{RX}^2}{2d^3} \int_0^{\infty} \frac{x^3 e^{-\left[\frac{xh}{d} + \sqrt{x^2 + j2\pi\mu_0 h f \sigma}\right]}}{x + \sqrt{x^2 + j2\pi\mu_0 h f \sigma}} dx \quad (65)$$

One can see in Gibson's model that when $\sigma = 0$, the mutual inductance reduces to that of two dipoles in air.

Figure 3.2 compares the two models when the transmitter is at a depth of $d = 19$ meters and at a height of $h = 1$ meter. Both coils are have the same radius of 50 cm and 35 turns. Both models agree with the dipole approximation in air at frequencies of 100 Hz or less. Forget's model (64) begins to decay after 100 Hz and is close to the far-field approximation whereas Gibson's model (65) remains similar to the dipole approximation until around 10 kHz before it drops off.

The curves were found by numerically evaluating the integrals in (64) and (65) using Python and the `integrate.quad` function in the Scipy library. For equation (64), an numerical problem occurs when $x = \Omega$. We mitigate this by splitting the integral in tow parts. The first part goes from 0 to Ω and the second part goes from Ω to infinity.

Alternatively a finite difference time domain simulator was built to validate Gibson's model. Key results of the analytical and FDTD models are shown next. The FDTD simulations were run with the receiver coil fixed horizontally at heights of 0.5 and 1 meter above the water's surface, while the transmitter is aligned horizontally and coaxial with the receiver, and at various transmitter depths similar to that shown in Fig. (3.3). Note that the bottom half of the computational domain is water with a conductivity (σ) of 4 S/m (seawater) and a relative permittivity (ϵ_r) of 81, the top half is air, and the air-water interface is located at 1 m in the z -direction.

Wait's Sommerfeld integral (65) was evaluated numerically using MATLAB's built-in `quad1()` function which uses adaptive Gauss/Lobatto quadrature [11]. A comparison of the results of these two models for the transmitter depths of 0.5, 1.0, 2.0, and 3.0 m and receiver heights of 0.5 and

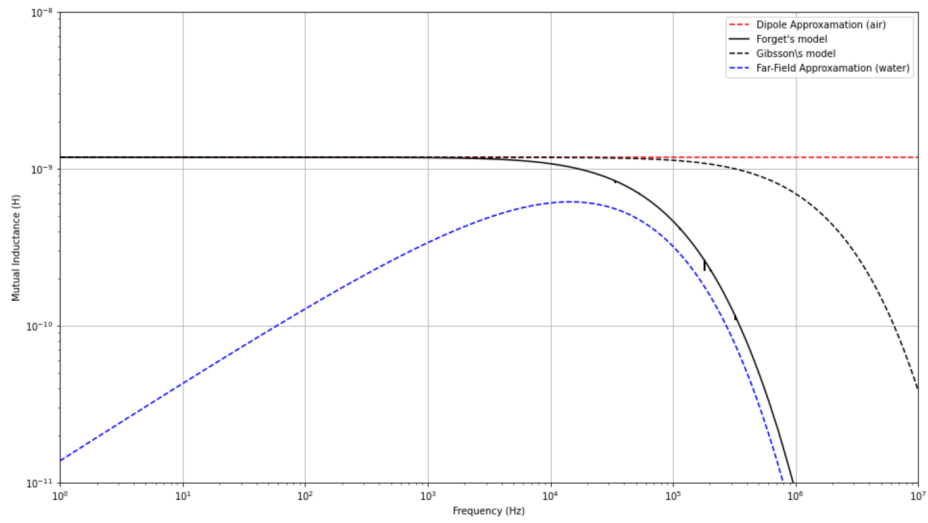


Fig. 3.2: Plots comparing Forget's model (64) to Gibson's (65) with $h = 1$ m, $d = 19$ m.

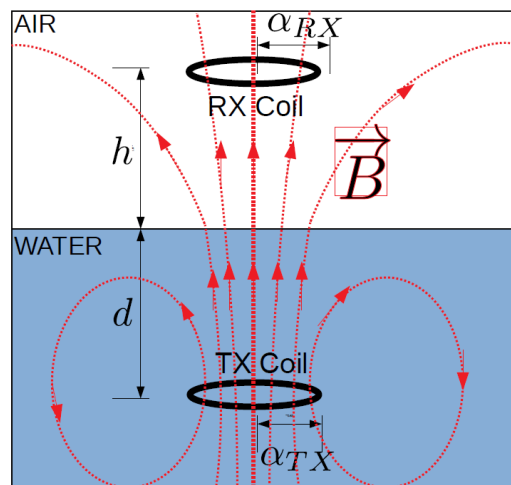


Fig. 3.3: Representation of the Magnetic Fields

1 m is shown in Fig. (3.4). The coils are assumed to have a 10 cm radius, the transmitting coil having 5 turns, the receiving coil having 5 turns, and the driving current has a maximum amplitude of 1 A.

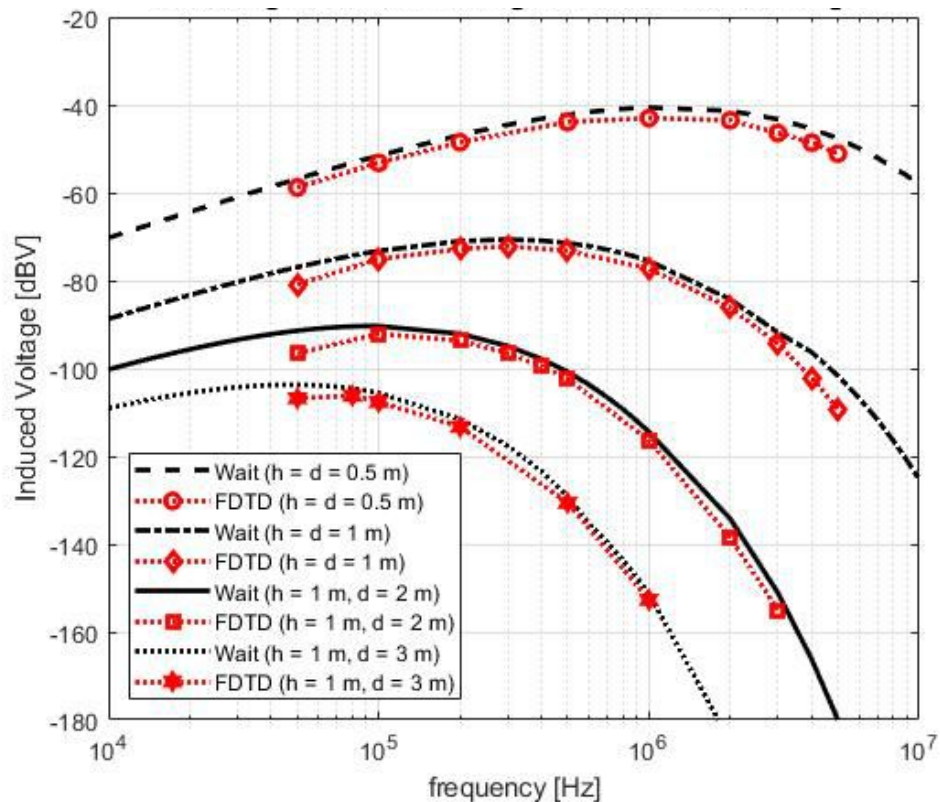


Fig. 3.4: Comparing the Predictions of the Induced Voltage in Receiver Coil Using Wait’s Analytical Model and the FDTD Simulations as a Function of Frequency, Transmitter Depths (d), and Receiver Heights (h).

Fig. (3.4) shows a good match between the FDTD simulation results and Wait’s analytical expression in terms of optimizing the center frequency for various coil configurations.

For the conditions shown, the simulated transmitter depth is limited to a maximum of 3 meters, and the induced voltage is below -100 dBV. In fact, to assess the potential for this link to reach the surface, an analysis of the channel capacity is run for different coil geometries in water. Using an approach developed in [12], the channel capacity as a function of frequency and distance is shown in Figure 3.5. It is found that by increasing the radius of the transmitter coil to 20 cm, and a number of turns equal to 35 would allow to reach the surface with a capacity close to 100 bps, for a center frequency close to 600 Hz.

3.2 Circuit Model

In this section, it is assumed that the mutual inductance is given by the model described by (64).

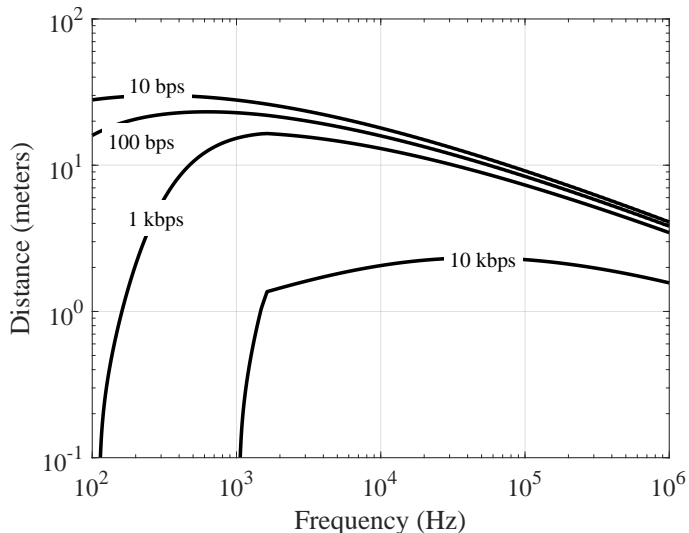


Fig. 3.5: Capacity of the magneto-inductive link

3.3 Frequency Dependence

A Python script was created to plot the transmission loss of the underwater to air MI system as a function of frequency. This code dynamically sets the values of the capacitors in order to always resonate. This is used to find the frequency that gives the largest gain in the system.

Figure 3.6 shows the modelled transmission loss for a node 10 meters below the sea surface. The dotted line gives the ideal loss, when the circuit is always assumed to resonate. This example suggests the capacitors can be set to resonate at $f_0 = 6.3$ kHz for the selected distance. The solid curve demonstrates the case if the resonance frequency is fixed at 6.3 kHz. For both curves, the effect of skin depth in water can be observed at frequencies on the order of 100 kHz.

3.4 Field Experiments

The original plan was to design and build an underwater test apparatus intended to test and validate the results of the analytical and FDTD models discussed above in the Summer of 2020; however, due to the recent social and political ramifications of the COVID-19 virus, the scheduling for these activities have been delayed. At the time of this writing, we expect to be able to test the magnetic induction link some time in the Fall, 2020. Unfortunately, this timeframe is just outside that of this report, so the results of those tests will not be included here. The results of those field experiments will be included in future work. This section will describe the development of the test platform to date and describe, how the tests will be conducted later this year.

3.4.1 Transmitter Design

The transmitter has been developed and an electronic design is being customized by the research team. A model of the circuit architecture is shown in Figure 3.7. At the transmitter, the coil is in series with a $R_{TX} = 4 \Omega$ resistor, and with a capacitor that ensures maximum gain at the operating frequency. Similarly, at the receiver, the coil forms a parallel resonant circuit with the receiver front-end.

A preliminary mechanical design for the electronic system is shown in Figure 3.9.

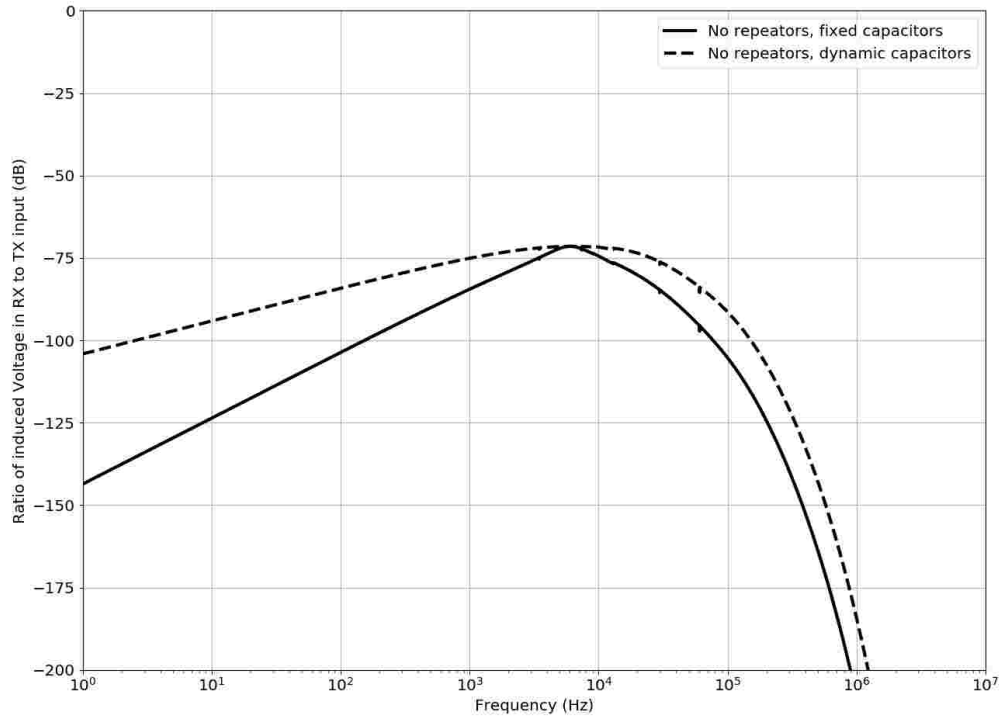


Fig. 3.6: Sample frequency response plot for a node 10 meters below the sea surface

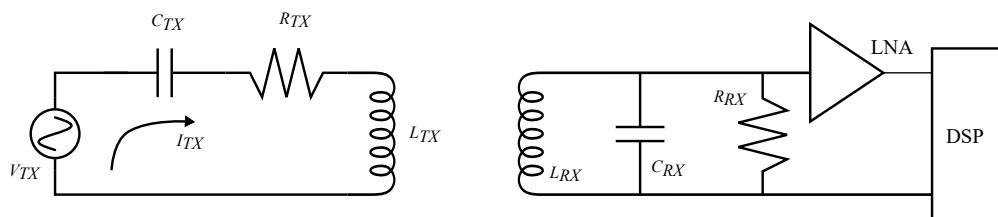


Fig. 3.7: Model of the system front-end

The input voltage will be supplied by a 24 V battery pack. Two DC/DC voltage regulators will be used to supply the positive and negative voltage rails for system power. The positive voltage rail will be supplied by the R-735.5P and the negative rail by the PTN78020A. The transmit signals are generated using a Zybo z7-20 development board which includes a 667 MHz dual-core ARM Cortex-A9 processor and a Xilinx 7-series FPGA. The power amplifier is the PA162u capable of 1.5 A output current and a bandwidth above 1 MHz. The tuning multiplexer block (Tuning MUX) consists of a capacitor bank and Single-Pole Double-Throw (SPDT) relays capable of withstanding the expected operating conditions and are intended to tune the transmitting coil to each of the frequencies of interest. The transmitter magnetic transducer consists of the three perpendicular coils shown in Fig. 3.8 intended to eliminate the dependence on the transmitter coil's orientation. This is a common approach in the literature.

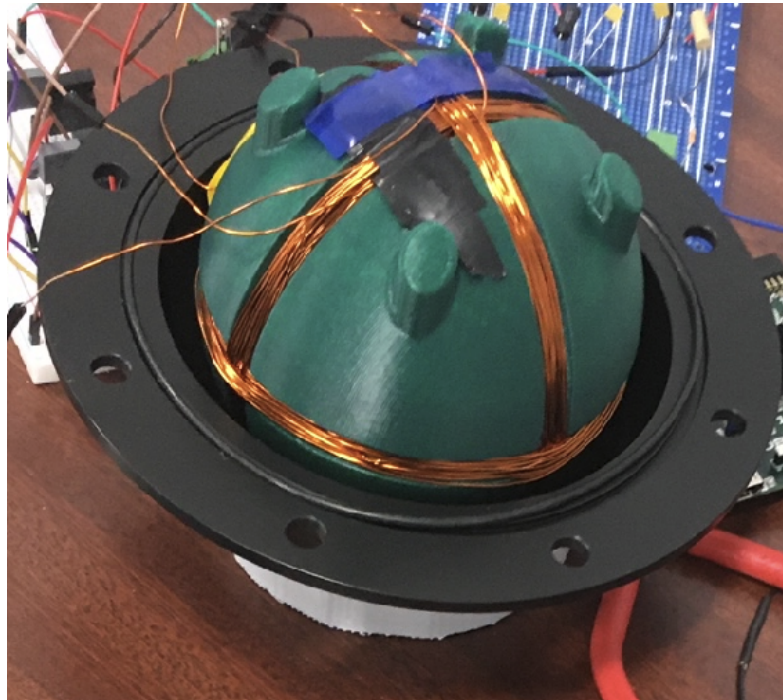


Fig. 3.8: Image of the interior of the transmitter

Also the control signals generated by the FPGA that allow to optimize the transmitter front-end are represented in Figure 3.10.

3.4.2 Receiver Design

Although, the full receiver design is not the objective of this work, a sensor is required to measure the voltage induced at the receiver. The receiving coil and tuning circuit is identical to that of the transmitter. The Low Noise Amplifier (LNA) is the LT1167 which has an easily adjustable gain, G determined by the resistor between the two R_g pins and is given by $G \approx 1 + 49 \text{ k}\Omega/R_g$. The Data Acquisition System (DAQ) is the NI-PCIe-6321 by National Instruments, which can sample at near 250 kHz which means our frequency of operation is limited by the Nyquist sampling criterion to around 125 kHz.

It was decided that a resonating tank circuit would be used to tune the receiving network, and LTspice simulations verify the need for this tuning. Figure 3.7 shows circuit model for

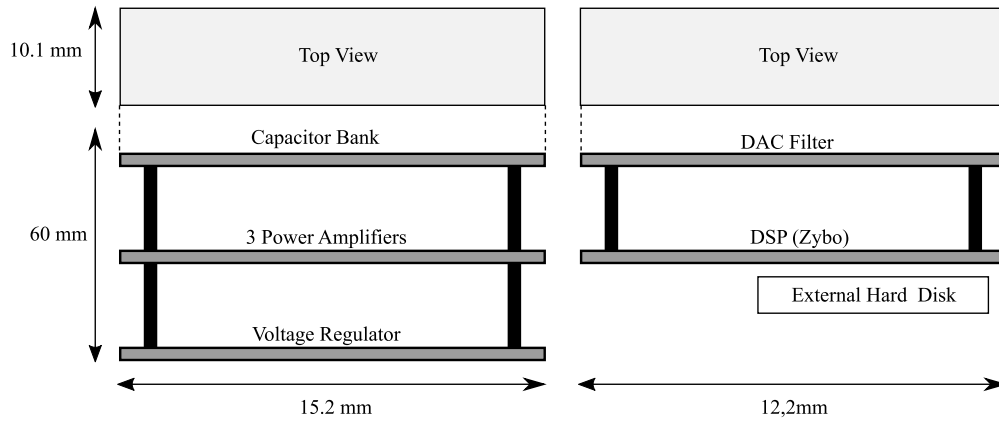


Fig. 3.9: Transmitter Electronic Board Design

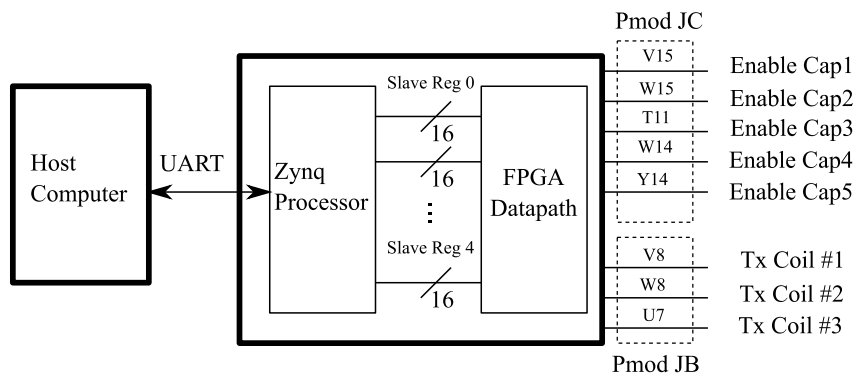


Fig. 3.10: Transmitter Firmware Interface to Generate Transmit Signals

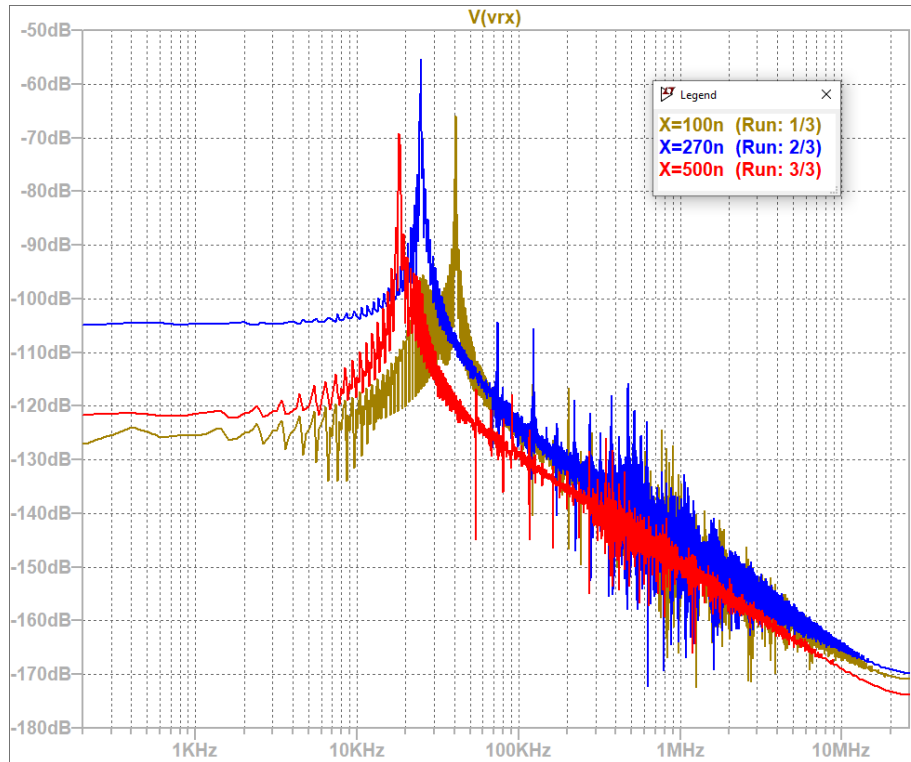


Fig. 3.11: System Frequency Response

simulations run in LTSpice. The transmitting circuit (consisting of V1, R1, C1, and L1) is tuned for near 25 kHz, and the resistance is equal to $R_{TX} = 4 \Omega$. The resonating tank circuit consists of L2 and C2 in the figure below. The value of C2 takes on values above, below, and at the capacitance value necessary for tuning the receiving coil for 25 kHz, which in this case is 270 nF for a 150 μH coil.

In Figure 3.11, the Fourier transforms of the signals induced in the receiving coil for each value of C2 is presented when a wideband pulse is injected into the transmitting circuit. It is clear the largest induced voltage occurs when the value for C2 equals 270 nF (the blue curve, run 2/3). The difference is as much as 15 dB, which translates to an increase in the size of the induced voltage on the order of 25 for these particular capacitor values. We want to ensure the received signal level is well above the noise floor, so having the ability to tune the receiving circuit for our frequency of operation is paramount.

3.4.3 Test Procedure

A test was run to validate the length of the communication link and while avoiding metallic interference. Dalhousie’s Aquatron provided adequate test locations.

The prototype of the tri-axial transmitter (figure 3.8), with a 6.25 cm radius was fabricated, served to validate the link model.

Figure 3.12 shows how the transmitter and receiver were deployed in the Aquatron. A long wooden stick is attached to a pontoon and is partially submerged underwater. At the bottom end of the stick is the transmitter encased in a spherical waterproof case. Weights are used to keep the transmitter aligned parallel to the surface. At the other end of the stick is the receiver on a green spherical ball. Both coils are connected to long wires that go to electric equipment

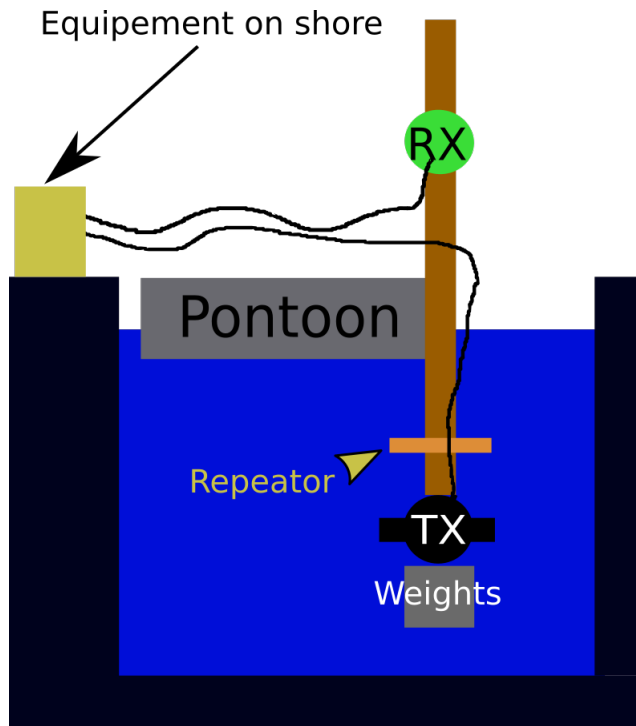


Fig. 3.12: Schematic of the Coils Setup in the Aquatron.

located on land. Figure 3.13 shows an photo of the setup in action.

Figure 3.14 shows the schematic of the equipment and figure 3.15 shows what the electronics look like. A signal generator is used to send a sinewave with the ability to change the frequency and amplitude in real time. This sinewave is boosted through a power amplifier to help draw more current in the transmitter. Then the signal is sent to the circuit (figure 3.7) which contains a removable capacitor that can be changed at any time in order to resonate at a given frequency. An oscilloscope is used to measure the wave the moment it leaves the power amplifier as well as the voltage across the resistor (used to calculate the current in the transmitter).

On the receiver side, the coil is sent to the circuit in figure 3.7. The voltage across the receiver resistor is wanted, but is too small to be measured directly. Therefore, the wanted signal is passed through a low noise amplifier with a gain of 100+ followed by an inverting amplifier which provides an additional gain of 50. The output of the second amplifier is what is recorded on the oscilloscope (same one as before).

All signals measured in the oscilloscope are recorded in a .csv file in a USB stick. For a given transmitter depth (1m, 2m, 3m) and a given resonance frequency (78 kHz, 24.8 kHz, 81 kHz), multiple sinewaves of different frequencies were sent and recorded on the oscilloscope. The amplitude on the signal generator was adjusted as necessary in order to output a proper sinewave and to be measured by the scope.

3.4.4 Preliminary Data Analysis

All of the .csv files recorded are stored and sorted on a computer based on the transmitter depth and the resonance frequency. The goal is to recreate resonance response plots similar to figure 3.6. To achieve this, at a given transmitter depth and resonance frequency, the frequency of operation and the measured voltage ratio must be found for each file and then plotted.

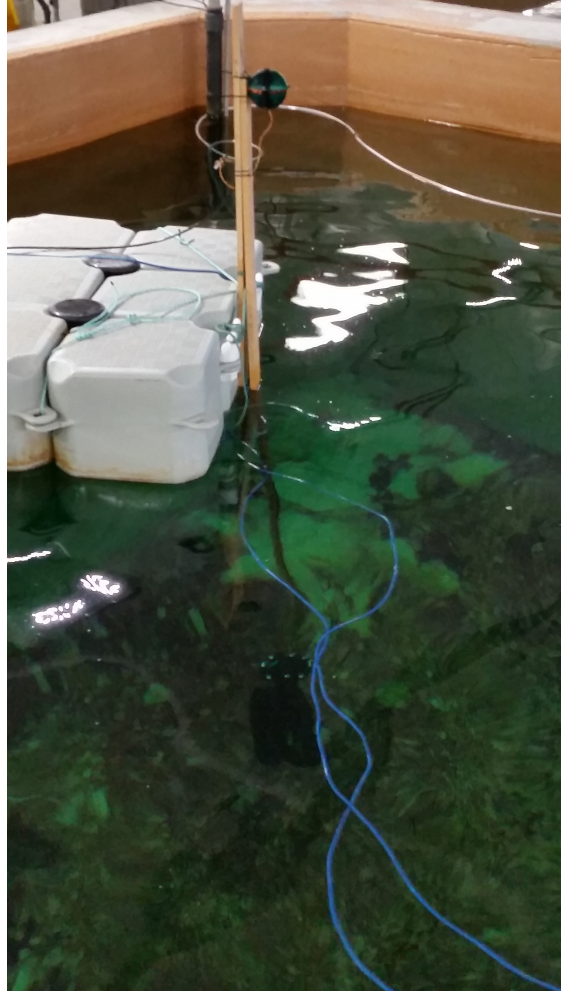


Fig. 3.13: Photo of the Test Setup.

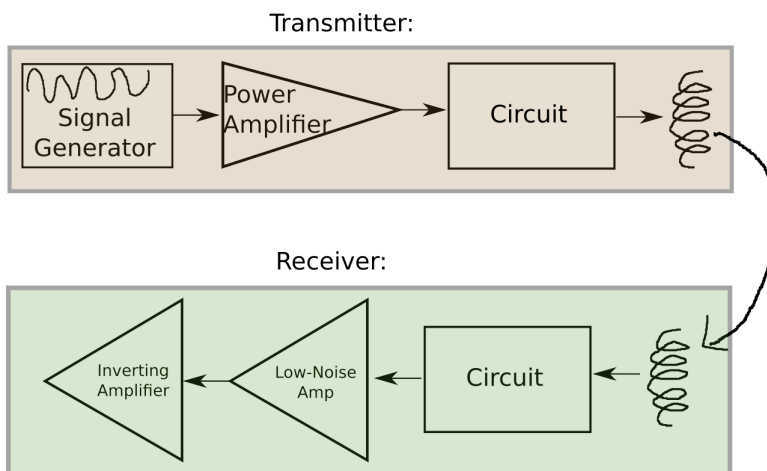


Fig. 3.14: Schematic of the Equipment.



Fig. 3.15: Photo of the Electronic Setup.

Each .csv file recorded four signals: The signal directly from the signal generator (can be used to verify the frequency), the signal voltage from the power amplifier (to measure the input voltage), the signal voltage from the TX resistor (used to measure the TX current), and the receiver voltage.

The process of finding the frequency for a given .csv file is found directly by the filename since careful attention was made to name the filename based on the frequency of operation. This can be verified by the first sinewave recorded.

For both the input voltage (second sinewave recorded) and the output voltage (fourth sinewave), the amplitudes are estimated in a Python script. The waves are first passed through a Butterworth bandpass filter to remove any noise from the signal. The first 20% of the filtered signal is ignored due to the unwanted effect of the filter. Then a least-squares fit is applied to estimate the amplitude of the signal. Figure 3.16 demonstrates how this filtering Python script works.

A sample of the resulting transmission loss graph is found in figure 3.17. Both plots are when the transmitter is 2 feet deep underwater. The 24 kHz plot has a larger gain at resonance when compared to the 81 kHz, but the quality factor is also bigger.

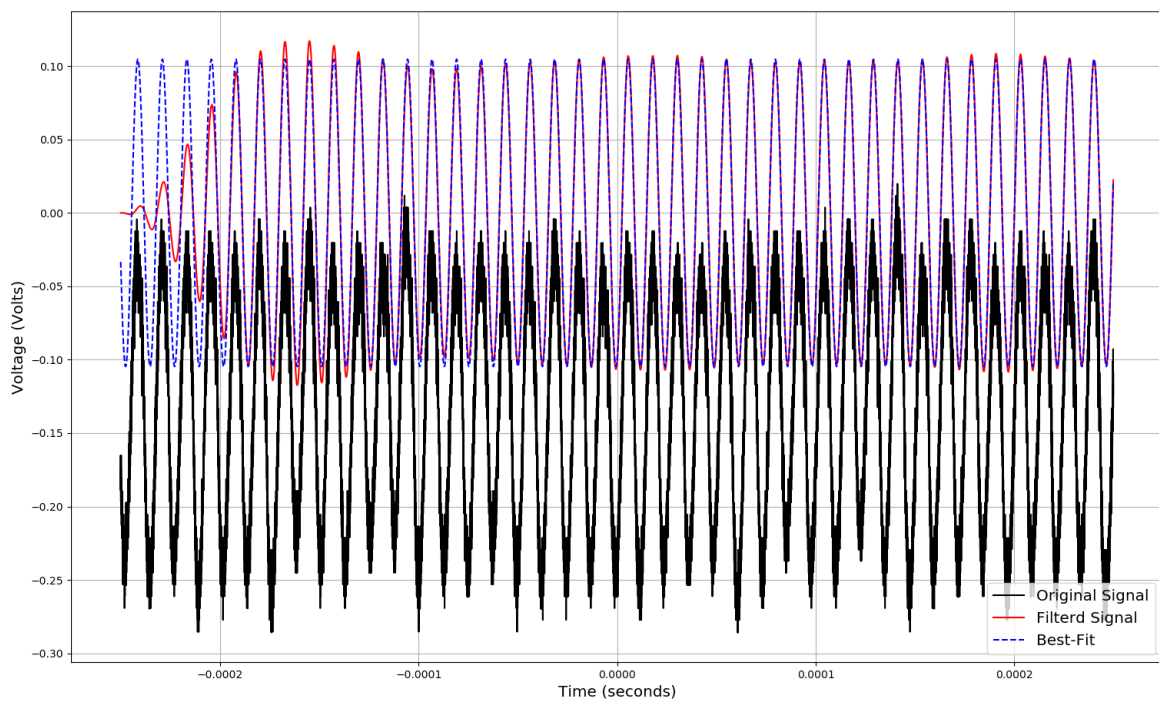


Fig. 3.16: Sample illustration of how the signal is passed through a bandpass filter and then a least-squares fit is applied.

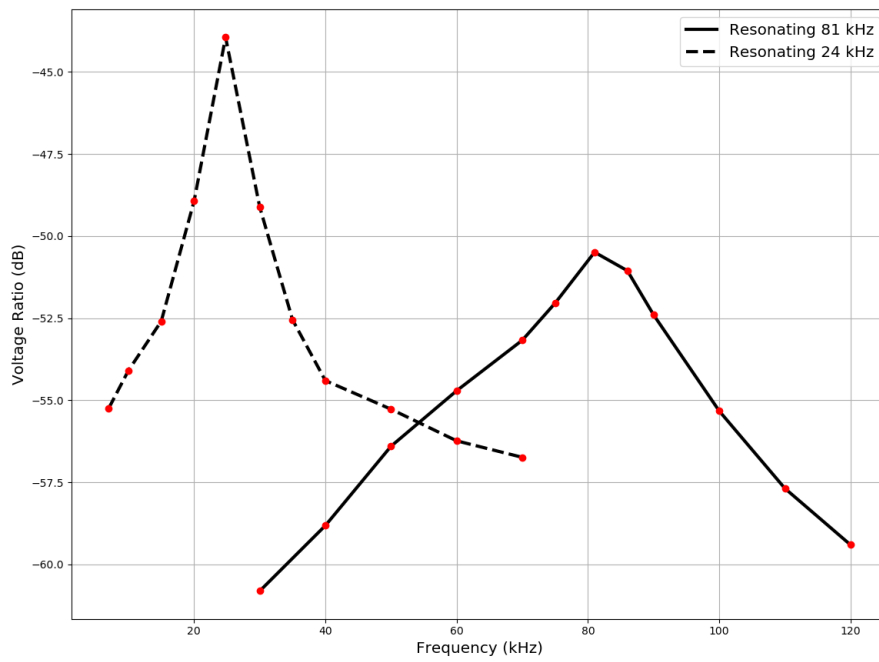


Fig. 3.17: Measured voltage ratio for a TX depth of 2 ft and at two resonating frequencies: At 24 kHz and at 81 kHz.

4 Conclusions and Impact

In this project, a real-time processing system has been developed to enable remote passive localization of harbour porpoises in the Bay of Fundy.

In order to integrate a complete system, first a low-complexity localization algorithm has been developed using a compact sensor array. The localization algorithm has been validated using marine mammal data collected during a 7-day trial in the Summer 2019, in the North side of Grand Passage, Nova Scotia. It was demonstrated that the algorithm can serve to track a vessel deployed at a given distance and bearing within a few hundred meters from the array. The algorithm was using a 47-kHZ sonar pulse as a representative signal source; it was found that while the bearing estimating was relatively accurate, the range estimation had a significant array. This was attributed to the planar geometry of the array. Further, the localization algorithm was applied to a harbour porpoise observed in the area, and the distance of the harbour porpoise was estimated to be approximately 627 meters, with a bearing of 60° with respect to the orientation of the array. To improve the accuracy of the range estimation, a new proposed array geometry was proposed, with 3 transducer elements disposed on a plane, and 2 additional elements located above.

To forward the information above the surface, in this project, magneto-inductive communication is proposed to cross the air water boundary. A model is developed, and a software reconfigurable transmitter physical layer is programmed on an FPGA that can forward the localization results to a node situated above the surface. The transmitter also includes a set of linear amplifiers that can provide a current of one Ampere, in each element of a tri-axial coil. The models indicate that to communicate between a node 5 meters below the surface, to a node 5 meters above the surface, the optimum frequency of operation is equal to approximately 7 kHz.

Proper operation of key components was confirmed through a deployment in Dalhousie's Aquatron test tanks. The magneto-inductive communication link was setup, and a short range link was validated for a transmitter located at approximately 2 meters below the surface, to a receiver 1 meter above the surface. A low transmission loss of 44 dB was reported for a communication link of 24 kHz. The measurements validate the simulation results, and can serve to optimize the dimensions of the coil for a node as low as 10 meters below the sea surface.

During the deployment in the Aquatron, the real-time localization hardware was also validated. Specifically, a new array geometry was attached to the recorder. Also, the protocol to enable real-time transmission between the recorder, and the localization hardware was tested. While the embedded processor architecture for the localization real-time system is finalized, the programming of the high-speed acoustic signal processing on FPGA is still under development. The latency of the system will be constrained on the hardware resources required by the FPGA.

5 Recommendations and Future Considerations

In this work, key components have been developed and tested to enable the deployment of remote localization system. Individually, each component shows great promise in being able to track harbour porpoises using the animal's vocalization, instead of an active sonar. A low-power implementation of the localization system can significantly reduce the deployment duration for the device.

The research team in the UW-STREAM lab at the Dalhousie is currently working with Fundy

Ocean Research Center for Energy to finalize the programming of the localization algorithm, and its deployment on the FAST platform in the Minas Basin in the summer 2021.

The real-time hardware system also includes a system to communicate to a node above the sea surface. To enable a link between a node 10 meters below the sea surface, and one above the surface, the transmitter must be re-designed and optimized for operation near 6 kHz, as predicted in simulation. Unfortunately, the 6 kHz front-end was unstable during the current tests.

References

- [1] Jacob Benesty, Jingdong Chen, and Yiteng Huang, *Microphone Array Signal Processing*, Springer Berlin Heidelberg, 2008.
- [2] Finn B. Jensen, William A. Kuperman, Michael B. Porter, and Henrik Schmidt, *Computational Ocean Acoustics*, Springer New York, 2011.
- [3] M. Hotkani, M. Seyedin, and J.-F. Bousquet, “Underwater object localization using the spinning propeller noise of ships based on the wittekind model,” *International Journal of Engineering and Advanced Technology*, vol. 9, no. 3, pp. 2736–2741, 2020.
- [4] Zoi-Heleni Michalopoulou, “The effect of source amplitude and phase in matched field source localization,” *The Journal of the Acoustical Society of America*, vol. 119, no. 3, pp. EL21–EL26, 2006.
- [5] Alexandra Tolstoy, *Matched field processing for underwater acoustics*, World Scientific., 1993.
- [6] A. B. Baggeroer, W. A. Kuperman, and Henrik Schmidt, “Matched field processing: Source localization in correlated noise as an optimum parameter estimation problem,” *The Journal of the Acoustical Society of America*, vol. 83, no. 2, pp. 571–587, 1988.
- [7] M. J. Irshad, Hangfang Zhao, and W. Xu, “High resolution matched-field source localization based on sparse-reconstruction,” in *2016 IEEE/OES China Ocean Acoustics (COA)*, 2016, pp. 1–5.
- [8] B. Jiang and F. h. Chen, “High precision time delay estimation using generalised mvdr cross spectrum,” *Electronics Letters*, vol. 43, no. 2, pp. 131–133, 2007.
- [9] Petre Stoica and Randolph L. Moses, *Introduction to spectral analysis*, Prentice-Hall, 1997.
- [10] Anne Villadsgaard, Magnus Wahlberg, and Jakob Tougaard, “Echolocation signals of wild harbour porpoises, *phocoena phocoena*,” *Journal of Experimental Biology*, vol. 210, no. 1, pp. 56–64, 2007.
- [11] D. Gibson, *Channel Characterisation and System Design for Sub-Surface Communications*, Lulu Enterprises, Leeds, Great Britain, 2010.
- [12] S. R. Padyath Ravindran, J. . Bousquet, and N. Gaoding, “Characterization of a 3d underwater magneto-inductive transmitter coil array,” in *OCEANS 2018 MTS/IEEE Charleston*, 2018, pp. 1–6.